

# A novel multitargeted self-assembling peptide-siRNA complex for simultaneous inhibition of SARS-CoV-2-host cell interaction and replication

Martina Tuttolomondo,<sup>1</sup> Stephanie Thuy Duong Pham,<sup>1</sup> Mikkel Green Terp,<sup>1</sup> Virginia Cendán Castillo,<sup>1</sup> Nazmie Kalisi,<sup>2</sup> Stefan Vogel,<sup>2</sup> Niels Langkjær,<sup>3,4</sup> Ulla Melchior Hansen,<sup>6</sup> Helge Thisgaard,<sup>3,4</sup> Henrik Daa Schrøder,<sup>4,5</sup> Yaseelan Palarasah,<sup>1</sup> and Henrik Jørn Ditzel<sup>1,4,7</sup>

<sup>1</sup>Department of Molecular Medicine, Unit of Cancer and Inflammation Research, University of Southern Denmark, 5000 Odense, Denmark; <sup>2</sup>Department of Physics, Chemistry and Pharmacy, University of Southern Denmark, 5000 Odense, Denmark; <sup>3</sup>Department of Nuclear Medicine, Odense University Hospital, 5000 Odense, Denmark; <sup>4</sup>Department of Clinical Research, University of Southern Denmark, 5000 Odense, Denmark; <sup>5</sup>Department of Pathology, Odense University Hospital, 5000 Odense, Denmark; <sup>6</sup>Department of Molecular Medicine, Imaging Core Facility, DaMBIC, University of Southern Denmark, 5000 Odense, Denmark; <sup>7</sup>Department of Oncology, Odense University Hospital, 5000 Odense, Denmark

**Effective therapeutics are necessary for managing severe COVID-19 disease despite the availability of vaccines. Small interfering RNA (siRNA) can silence viral genes and restrict SARS-CoV-2 replication. Cell-penetrating peptides is a robust method for siRNA delivery, enhancing siRNA stability and targeting specific receptors. We developed a peptide HE25 that blocks SARS-CoV-2 replication by various mechanisms, including the binding of multiple receptors involved in the virus's internalization, such as ACE2, integrins and NRP1. HE25 not only acts as a vehicle to deliver the SARS-CoV-2 RNA-dependent RNA polymerase siRNA into cells but also facilitates their internalization through endocytosis. Once inside endosomes, the siRNA is released into the cytoplasm through the Histidine-proton sponge effect and the selective cleavage of HE25 by cathepsin B. These mechanisms effectively inhibited the replication of the ancestral SARS-CoV-2 and the Omicron variant BA.5 *in vitro*. When HE25 was administered *in vivo*, either by intravenous injection or inhalation, it accumulated in lungs, veins and arteries, endothelium, or bronchial structure depending on the route. Furthermore, the siRNA/HE25 complex caused gene silencing in lung cells *in vitro*. The SARS-CoV-2 siRNA/HE25 complex is a promising therapeutic for COVID-19, and a similar strategy can be employed to combat future emerging viral diseases.**

## INTRODUCTION

Since 2019, SARS-CoV-2 has caused the global COVID-19 pandemic, impacting public health and the economy.<sup>1</sup> This virus spreads through the respiratory system, leading to lung damage, inflammation, and potentially fatal respiratory failure.<sup>2</sup> Treatments like dexamethasone, interleukin (IL)-6 monoclonal antibodies (e.g., tocilizumab), RNA polymerase inhibitors (e.g., Remdesivir, Nirmatralvir/Ritonavir), and Spike protein receptor binding

domain (RBD) monoclonal antibodies have been used to alleviate symptoms in hospitalized COVID-19 patients, including lung injury reduction.<sup>3–6</sup> However, these treatments have limitations such as variable effectiveness, side effects, and reduced efficacy against new variants. Moreover, combining multiple drugs raises toxicity and side effect risks.<sup>7,8</sup> These challenges underscore the necessity for continuous research and the development of new COVID-19 treatments.

Efforts to refine COVID-19 therapeutics continue, with vaccines advancing significantly,<sup>9</sup> but emerging SARS-CoV-2 variants and antigenic drift challenge their long-term efficacy.<sup>10,11</sup> Vaccines updated for new variants may be less effective due to antigenic imprinting wherein the immune system prefers previous infection responses.<sup>12</sup> Despite effective vaccines and antivirals, new variants often evade existing protections. The ongoing development of antivirals reduces COVID-19 severity, but more specific and effective treatments are needed.

Several specific anti-COVID-19 treatments are in development, including promising small interfering RNA (siRNA)-based therapies.<sup>13–15</sup> These siRNAs, utilizing the RNA interference (RNAi) machinery, degrade viral RNAs and can be swiftly adapted to target emerging variants.<sup>10,16</sup> There is significant interest in RNAi-based therapeutics for COVID-19, especially targeting the

Received 13 April 2023; accepted 22 May 2024;  
<https://doi.org/10.1016/j.omtn.2024.102227>.

**Correspondence:** Martina Tuttolomondo, Department of Molecular Medicine, Unit of Cancer and Inflammation Research, University of Southern Denmark, 5000 Odense, Denmark.

**E-mail:** [mtuttolomondo@health.sdu.dk](mailto:mtuttolomondo@health.sdu.dk)

**Correspondence:** Henrik Jørn Ditzel, Department of Molecular Medicine, Unit of Cancer and Inflammation Research, University of Southern Denmark, 5000 Odense, Denmark.

**E-mail:** [hditzel@health.sdu.dk](mailto:hditzel@health.sdu.dk)



viral RNA-dependent RNA polymerase (RdRp), a key replication enzyme.<sup>17</sup> RdRp-targeting siRNA sequences have been screened for optimal gene silencing.<sup>9,10,16</sup>

As a result of their instability in the bloodstream, siRNA molecules must be combined with a vehicle that prohibits their renal clearance and protects them from degradation by serum RNases.<sup>18</sup> Several vehicles, including lipid nanoparticles and dendrimers, are being considered for administering SARS-CoV-2 siRNAs.<sup>9,10,16</sup> Among the other siRNA vehicles, cell-penetrating peptides have multiple advantages, including spontaneous siRNA encapsulation and the possibility of designing their sequence to bind a specific receptor and target a specific cell type or tissue.<sup>19–24</sup> Furthermore, similar to antibodies, short peptides can be designed to block a viral receptor on the cell membrane and prevent virus internalization.<sup>25</sup>

Early in the pandemic, it was found that SARS-CoV-2 enters lung cells via its spike protein interacting with the host's ACE2 enzyme.<sup>26,27</sup> The sequence of the viral S protein interacting with ACE2 has been named RBD (receptor binding domain).<sup>28</sup> More recent studies have shown that several other cell receptors are involved in SARS-CoV-2 internalization. Several integrins have been proven to act as co-receptors by recognizing an RGD sequence of the viral S protein.<sup>29–32</sup> In addition, the transmembrane glycoprotein neuropilin-1 (NRP1), which promotes the endocytosis of activated integrins, has been recently identified as a receptor for SARS-CoV-2 infection.<sup>33</sup> Finally, it has been established that after the endocytosis of the SARS-CoV-2 virion, the endo-lysosomal escape of replicated viruses occurs through the proteolytic activity of cysteine cathepsins B and L.<sup>34,35</sup>

In previous studies, we developed DMBT1-derived peptides capable of siRNA encapsulation and cell penetration.<sup>36–39</sup> In this study, we developed a lung-targeting HE25 peptide that, in complex with a siRNA against SARS-CoV-2, can inhibit the replication of SARS-CoV-2 up to 100% *in vitro*. *In vivo*, HE25 and its complex with SARS-CoV-2 siRNA accumulate in mouse lungs indicating its potential as a therapeutic for reducing COVID-19 lung infection.

## RESULTS

### HE25 allows efficient siRNA encapsulation through a combination of electrostatic and hydrophobic interactions, and hydrogen bonding

In previous studies, we demonstrated that peptides derived from the pattern recognition protein DMBT1 and containing the GRVRVLR domain allowed siRNA encapsulation by a self-assembly mechanism.<sup>38,39</sup> Here, we designed a modified DMBT1-derived peptide, HE25 (sequence: stearyl-HEHHEHHEHEHGFLGRVRVLRGDKWamide), that, after incubation at 50°C, exhibits 3-fold more effective encapsulation of siRNA compared with the previously designed DMBT1-derived peptides, as determined at a peptide:siRNA molar ratio 1:20 by electrophoretic mobility shift assay (Figure 1A, top right panel). To systematically investigate the interaction forces between

siRNA molecules targeting SARS-CoV-2 RdRp and the peptide HE25, we employed an electrophoretic mobility shift assay (EMSA) (Figure 1A) using varying siRNA:peptide molar ratios and examined these interactions under diverse conditions, including different temperatures and pH levels. Additionally, we explored the influence of various destabilizing agents, namely dextran sodium sulfate (DSS), NaCl, and urea introduced both before and after the encapsulation process. This comprehensive analysis aimed to elucidate the molecular dynamics that govern the stability and efficacy of the siRNA-HE25 complex in varying environmental and experimental conditions. Our findings demonstrate that, at pH 7 and temperatures from 4°C to 37°C, HE25 binds to siRNA at a molar ratio of 1:40 and effectively encapsulates it at a 1:100 siRNA:peptide molar ratio (Figure 1A, top panels). Notably, at pH 7 the encapsulation efficiency significantly increases at 50°C, suggesting that thermal energy may induce favorable conformational changes in the peptide or siRNA, thereby enhancing their interaction. Additionally, at this pH and temperature, 20 mg/mL DSS was observed to interfere with the binding and disassemble the preformed complex, indicating a potential electrostatic competitive interaction with the siRNA backbone (Figure 1A, bottom panels). Conversely, 1.6 M urea hindered initial binding but did not affect the ones formed, suggesting its ability to hinder hydrogen bonding is limited to the early stages of interaction. Interestingly, 4% NaCl showed no notable effect on either binding or disassembly, implying that ionic strength or charge shielding plays a minor role in complex stability. At pH 7 and 4°C, similar DSS interference as at 50°C was observed, while the effect of urea was not observed before encapsulation, meaning that hydrogen bonding is more involved at high temperatures. At pH 4 and 50°C, DSS hindered the siRNA:peptide complex stability only after complex formation.

Further insights on the peptide-siRNA interaction forces were gained from *in silico* docking studies (Figure 1B), which revealed pseudobonds between the peptide domain GVRVLXXXW and the siRNA backbone. More specifically, the interaction was observed between tryptophan and arginine residues and the nucleic acid backbone of the siRNA. These findings suggest a key role for hydrophobic interactions possibly involving tryptophan, and electrostatic interactions facilitated by arginine, in stabilizing the peptide-siRNA complex. Our results indicate that a combination of hydrophobic interactions, electrostatic forces, and hydrogen bonding contribute to the complex's stability. These interactions appear to be highly dependent on both the conformation of the peptide and the structural integrity of the siRNA, as evidenced by the temperature and pH-dependent binding efficiencies and the differential effects of DSS and urea.

### Size, charge, and morphological analysis of SARS-CoV-2 siRNA/HE25 complexes across various molar ratios and storage conditions

Next, we characterized the SARS-CoV-2 siRNA/HE25 complex at various molar ratios in terms of its size, zeta potential, and morphology (Figure 2). Utilizing nano tracking analysis, we measured

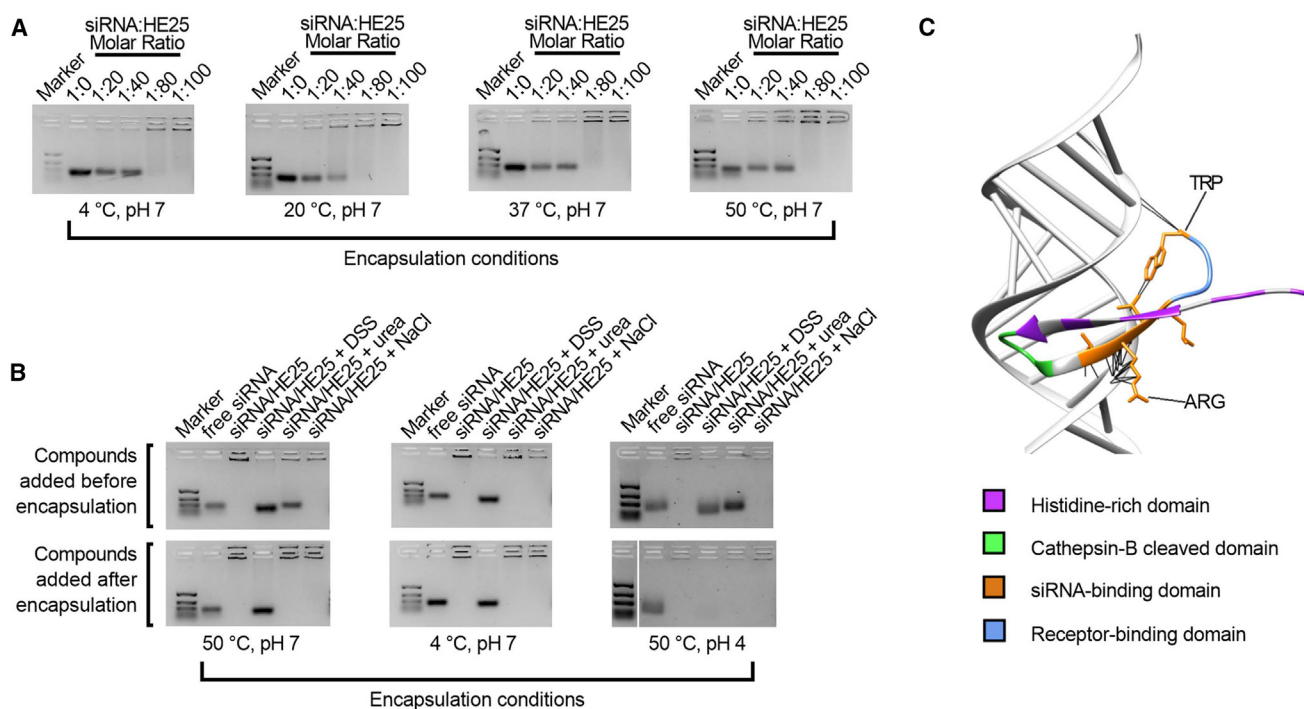


**Figure 1. HE25-mediated siRNA encapsulation and interaction force**

(A) Electrophoretic mobility shift assay showing siRNA encapsulation by HE25 across varying molar ratios and temperatures. (B) Assay results illustrating the interaction forces in siRNA encapsulation by HE25, with DSS, urea, or NaCl added both before (top gels) and after (bottom gels) encapsulation, conducted at a molar ratio of 1:100 and various temperature/pH levels to evaluate stability and binding efficiency. (C) *In silico* modeling showing the interaction between HE25 and siRNA, visualized through docking analysis. Pseudobonds between molecules are highlighted in black.

the hydrodynamic diameter and charge of the complexes both immediately after preparation (day 1) and after a storage period of 15 days at 4 °C. These measurements were conducted in ultrapure water and a solution containing 1% PEG2000.

Our results indicated that, in ultrapure water, the complexes consistently exhibited a hydrodynamic diameter of approximately 100 nm across all tested molar ratios (Figure 2A, black bars). The particles demonstrated a low full width at half maximum (FWHM), indicating a narrow size distribution, which is a key indicator of low polydispersity in the samples (Figure 1C, black series). Notably, there was an observed increase in charge from approximately 0 to 30 mV correlating with higher siRNA:peptide molar ratios (Figure 2C, black series). However, during the 15-day storage period at 4 °C in ultrapure water, a slight aggregation of particles was observed, which doubled their hydrodynamic diameter and increased the polydispersity (Figure 2A, red bars, S1A, and S1C). Concurrently, a slight decrease in charge was also recorded (Figure 2C, red series, S1B).

Remarkably, the stability issue observed in ultrapure water was effectively mitigated by the addition of 1% PEG2000 to the storage solution (Figures 2B and 2D). This addition prevented the aggregation of particles and maintained the stability of the hydrodynamic diam-

eter and polydispersity over the 15-day storage period (Figures 2B and S1D). The charge increased to approximately 20–25 mV consistently across the molar ratios, indicating that the PEG adsorbed to the particle surfaces and stabilized them during storage, unmasking the siRNA/HE25 complex positively charged domains (Figure 2D). Transmission electron microscopy (TEM) revealed particle morphologies characterized by compact and rounded shapes, with sizes ranging between approximately 50 and 100 nm (Figure 2E). Notably, all particles demonstrated consistent spherical morphology across the different molar ratios, with some clustering at molar ratios 1:100 and 1:200.

#### Optimized serum stability and gene silencing: Advanced FRET analysis of siRNA/HE25 complexes across different serum environments and molar ratios, with demonstrated silencing efficacy in Vero E6 cells

The stability of peptide-siRNA complexes in serum is an important factor for its *in vivo* use. To examine this, we employed a fluorescence resonance energy transfer (FRET) kinetic assay to measure the FRET-siRNA stabilization in combination with our previously developed FRET-EMSA used to examine the FRET-siRNA/HE25 complex stability (Figures 3A–3D).<sup>40,41</sup> We found that the HE25 efficiently protected the FRET-siRNA from RNase degradation in fetal bovine serum (FBS) and mouse serum at all molar ratios

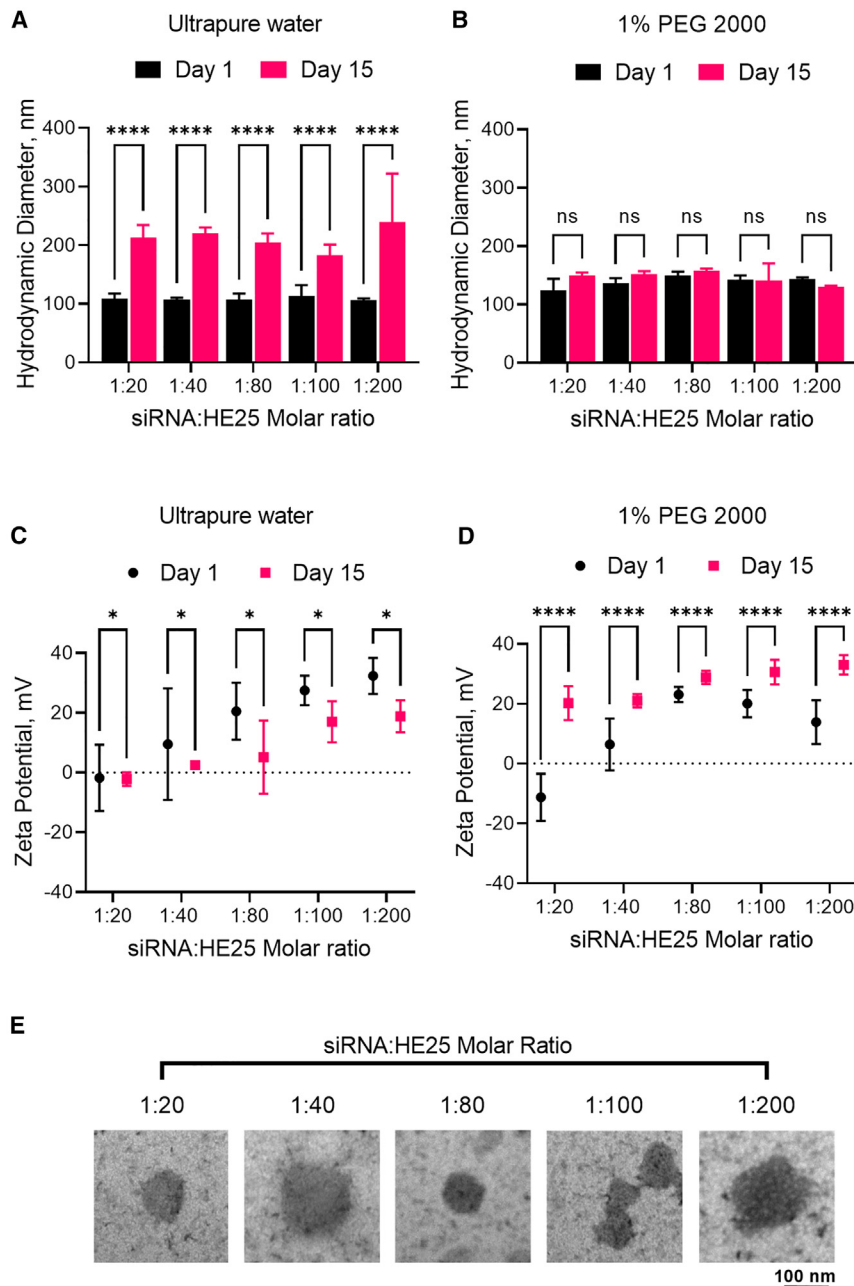


**Figure 2. Characterization of SARS-CoV-2 siRNA/HE25 complex: Size, charge, stability, and morphology analysis**

(A) Nano tracking analysis revealing the hydrodynamic diameter of the SARS-CoV-2 siRNA/HE25 complex on day 1 and day 15, stored at 4°C in ultrapure water and (B) in 1% PEG2000, across varied molar ratios. (C) Zeta potential measurements displaying the charge profile of the complex on day 1 and day 15 under the same storage conditions in ultrapure water and (D) in 1% PEG2000, at different molar ratios. (E) Transmission electron microscopy (TEM) images depicting the morphology of the SARS-CoV-2 siRNA/HE25 complex at various molar ratios. Error bars indicate mean  $\pm$  SD based on three stock replicates. Data were analyzed using GraphPad Prism, employing a two-way ANOVA and multiple comparison tests (\* $p < 0.0332$ ; \*\* $p < 0.0021$ ; \*\*\* $p < 0.0002$ ; \*\*\*\* $p < 0.0001$ ) for statistical significance evaluation.

manner in Vero cells, and approximately 85% silencing was observed at a siRNA concentration of 25 nM.

#### Cell uptake of siRNA/HE25 complex occurs via integrin binding followed by clathrin-mediated endocytosis

To investigate the uptake mechanism of the peptide-siRNA complexes in human cells, internalization pathway inhibitors were administered to Vero cells in parallel with different molar ratios of HE25 in complex with a GAPDH targeting siRNA. GAPDH silencing was significantly disrupted by chlorpromazine (clathrin inhibitor) and dynasore (dynamin inhibitor), but not by nystatin (caveolin inhibitor) or cytochalasin D (actin inhibitor, interfering with phagocytosis and macropinocytosis), indicating that the complex uptake occurs by clathrin-mediated receptor-mediated endocytosis (Figure 4A).

Furthermore, quantitative analysis using ImageJ was performed to evaluate the colocalization of Alexa Fluor 555-tagged siRNA/HE25 complex administered to Vero E6 cells with various endosomal markers. This analysis, derived from confocal microscopy images, provided a detailed assessment of the complex's interaction with cellular components at different molar ratios (Figure 4B). The quantitative data revealed similar patterns of interaction between the siRNA/HE25 complex and the endosomal markers: Rab 4 (early endosomes), Rab 9 (late endosomes), Rab11A (recycling endosomes), and Integrin Alpha V (ITGAV). The colocalization of the Alexa Fluor 555-tagged siRNA/HE25 complex with all observed cellular compartments

(Figures 3A and 3C). Furthermore, the peptide-siRNA complex at 1:100 was not disassembled in FBS and FRET-siRNA complex was intact after forced disassembling (Figure 3B). Moreover, HE25 protected the FRET-siRNA complex in human serum at molar ratios over 1:40 (Figure 3D).

Next, we evaluated whether GAPDH siRNA/HE25 complexes allowed efficient gene silencing *in vitro* using a KDaAlert GAPDH kit (Figures 3E, 3F; S2). This analysis showed the GAPDH siRNA led to gene silencing in a molar ratio or dose-response-dependent

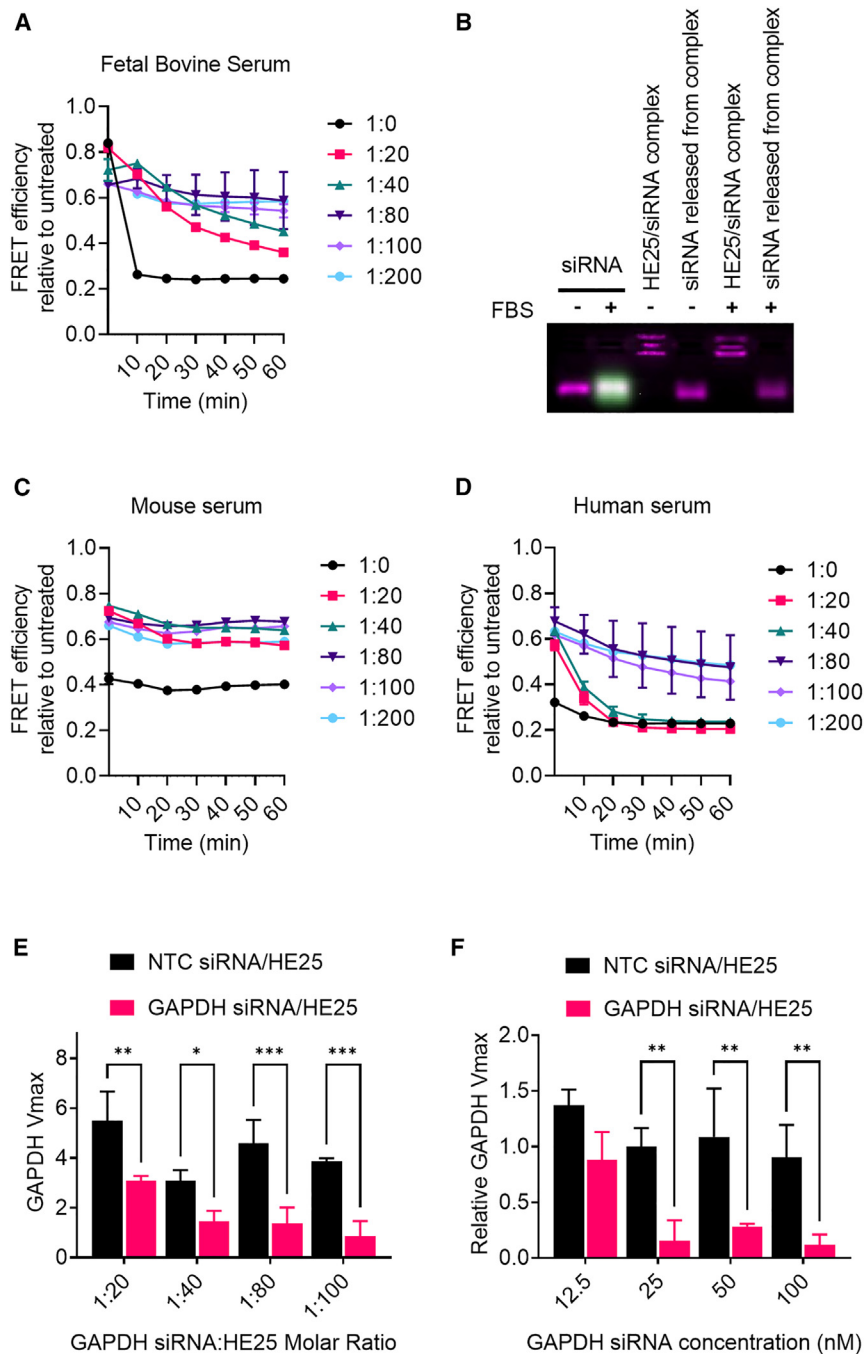


**Figure 3. Stability of siRNA/HE25 complexes in FBS and mouse and human serum, and silencing efficacy in Vero E6 cells**

(A) Fluorescence resonance energy transfer (FRET) kinetic assay at various siRNA/HE25 molar ratios, assessing FRET-tagged siRNA stability in 2.5% fetal bovine serum over time. (B) FRET electrophoretic mobility shift assay of siRNA/HE25 at a 1:100 M ratio, evaluating the stability of FRET-siRNA in 2.5% fetal bovine serum. Red lanes indicate intact siRNA, green lanes indicate degradation and siRNA band shifts upon peptide complexing signal interaction and stability. (C) FRET kinetic assay across different siRNA/HE25 molar ratios showing FRET-siRNA stability in 2.5% mouse serum and (D) in human serum. (E) GAPDH silencing efficacy in Vero E6 cells by GAPDH siRNA/HE25 complex at varied molar ratios, and (F) across different siRNA concentrations. Error bars indicate mean  $\pm$  SD based on three biological replicates. Data were analyzed using GraphPad Prism, employing a two-way ANOVA and multiple comparison tests ( $p < 0.0332$ ;  $**p < 0.0021$ ;  $***p < 0.0002$ ;  $****p < 0.0001$ ) for statistical significance evaluation.

**HE25 binds and inhibits recombinant SARS-CoV-2 spike protein and ACE2, ITGA2, and ITGAV cell receptors and is selectively degraded by the late endosomal cathepsin B leading to release of the siRNA**

In addition to ACE2, the main receptor targeted by SARS-CoV-2 spike protein is integrins, which have been demonstrated to bind the RGD motif of the spike protein.<sup>31,32</sup> Moreover, it has been shown that Neuropilin-1 facilitates SARS-CoV-2 cell entry and infectivity.<sup>33</sup> Peptides containing the NRP1 binding domain RXXR at the C terminus (C end) are designated CendR peptides.<sup>42</sup> The HE25 peptide sequence was designed to contain an integrin-binding RGD domain (RGDK) and an NRP1-binding CendR domain (RVLR). Enzyme-linked immunosorbent assay (ELISA) analysis of HE25-coated plates revealed that the peptide was recognized by Neuropilin-1 (NRP1), angiotensin-converting enzyme 2 (ACE2), Integrin  $\alpha 5$  (ITGA5), Integrin  $\alpha V$  (ITGAV), and spike RBD (Figures 5A and 5C). Integrin  $\beta 3$  (ITGB3), Integrin  $\alpha 2$  (ITGA2), Integrin  $\alpha 2B$  (ITGA2B), and the lung epithelial membrane protein FIB were included in the assay as negative controls to exclude unspecific receptor binding of HE25. In a different ELISA assay setup, we confirmed that spike RBD bound to ACE2, ITGAV, and ITGA2 (Figure 5B). Further, as described above, immunofluorescence staining of Vero cells revealed colocalization of AlexaFluor 555-labeled siRNA/HE25 complex with ITGAV (Figure 4C). The fact that HE25 binds ITGAV and ITGA5 receptor and that siRNA/HE25

was found to escalate in tandem with increasing molar ratios, suggesting a proportional enhancement in cellular uptake relative to the molar ratio. Figure 4C shows the colocalization at 1:40 M ratio. For control data and whole images related to this experiment, refer to Figures S3 and S4, respectively. Overall, these results, grounded in robust quantitative analysis and visually supported by confocal imaging, offer significant insights into the cellular interactions and mechanisms of action of the siRNA/HE25 complex.

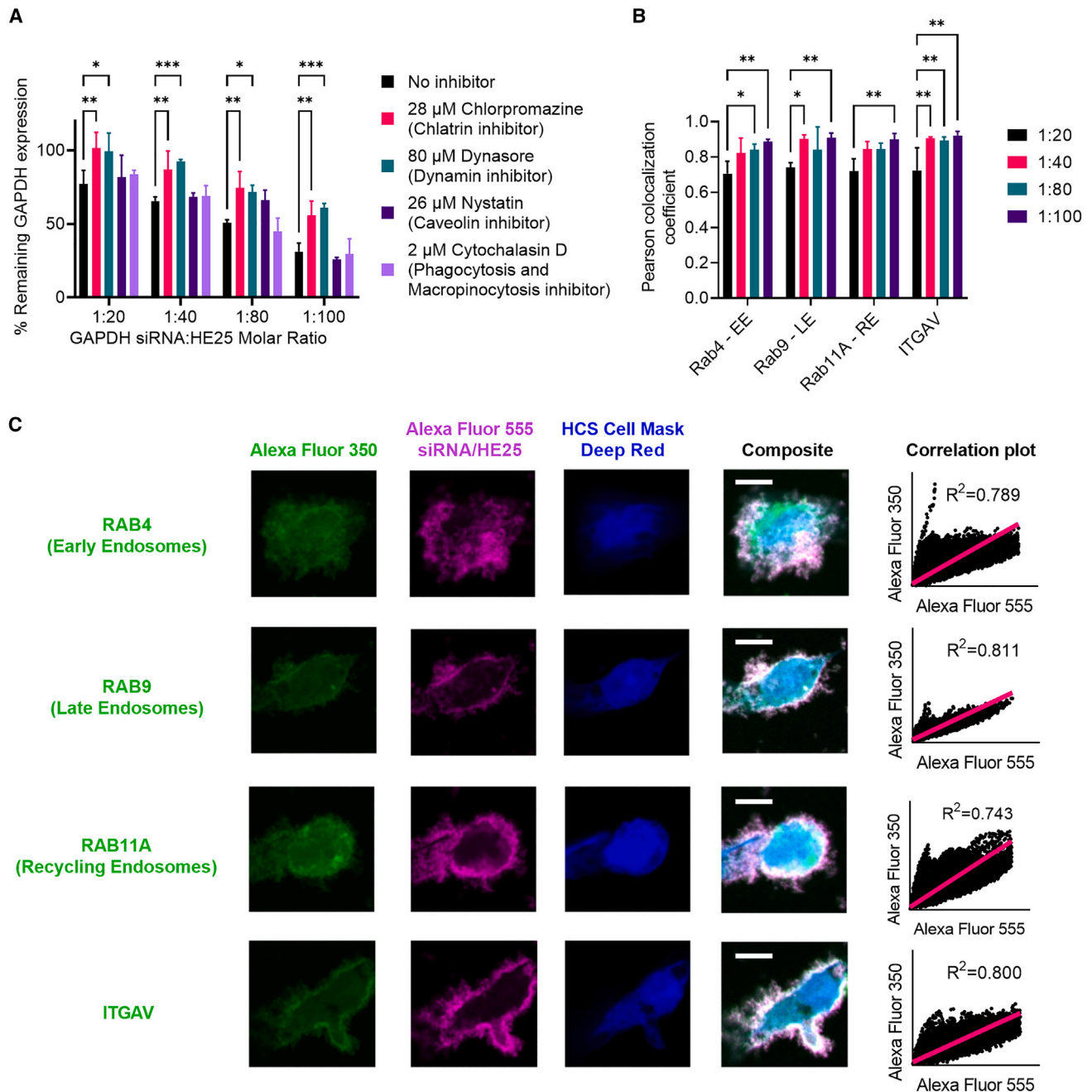


**Figure 4. Internalization mechanisms of siRNA/HE25 in Vero E6 cells**

(A) Assessment of GAPDH silencing in Vero E6 cells by GAPDH siRNA/HE25 complex across various molar ratios, using different internalization pathway inhibitors. (B) ImageJ quantitative analysis of colocalization from confocal microscopy images at diverse molar ratios. (C) Analysis of colocalization between Alexa Fluor 555-tagged siRNA/HE25 complex and Rab 4, Rab 9, Rab11A (markers for early, late, and recycling endosomes) or Integrin Alpha V (ITGAV). Selected cells are shown at a magnification of 5 $\times$  from a representative biological replicate at a 1:40 M ratio. Non-magnified images are available in [Figure S3](#). Rab4, Rab9, Rab11A, or ITGAV are shown in green pseudocolor (first column panels); Alexa Fluor 555 siRNA/HE25 in magenta pseudocolor (second column panels); and HSC Cell Mask Deep Red representing cell nuclei and cytoplasm in blue pseudocolor (third column panels). Areas of colocalization between green and magenta are depicted in white, signifying the spatial interaction between the siRNA/HE25 complex and endosomal or ITGAV markers. Pseudocolors were selected to enhance accessibility for individuals with color vision deficiencies. The scale bar in the upper right corner of the composite panels represents 5  $\mu$ m. Error bars indicate mean  $\pm$  SD based on three biological replicates. Data were analyzed using GraphPad Prism, employing a two-way ANOVA and multiple comparison tests ( $*p < 0.0332$ ;  $**p < 0.0021$ ;  $***p < 0.0002$ ;  $****p < 0.0001$ ) for statistical significance evaluation.

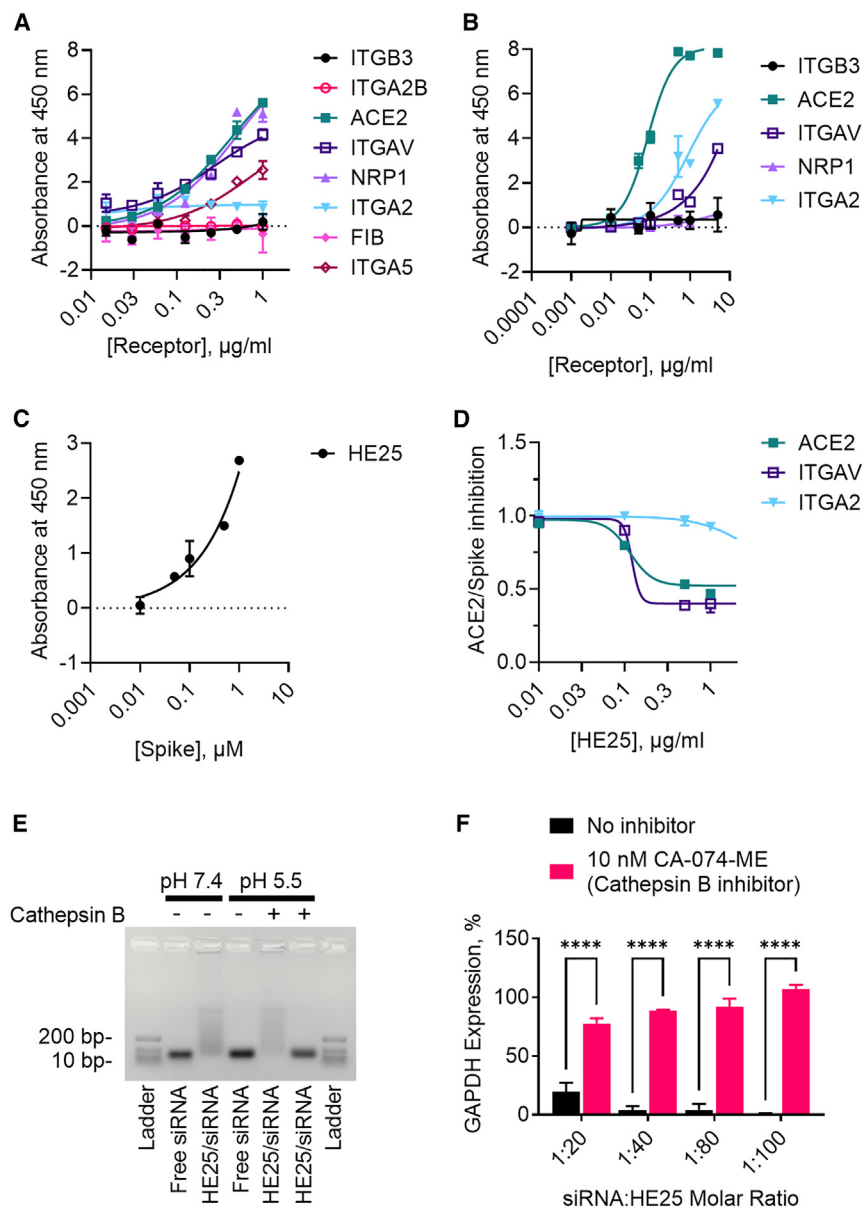


**Figure 5. Analysis of siRNA/HE25 complex receptor binding, SARS-CoV-2 cellular receptor inhibition, and endosomal release**

(A) Binding of HE25 to ACE2, ITGAV, NRP1, and ITGA5 as analyzed by ELISA. ITGB3, ITGA2, ITGA2B, and FIB were included as negative controls. (B) Receptors binding to SARS-CoV-2 spike RBD. (C) ELISA showing HE25 binding to SARS-CoV-2 spike RBD. (D) Competitive ELISA showing the inhibition of spike RBD binding to ACE2 and ITGAV receptors by increasing concentrations of HE25. ITGA2 receptor was used as a negative control. (E) EMSA showing the release of the siRNA from the complex in the condition of late endosome. Lanes 1 and 7 contain ladder; lanes 2 and 3 contain free siRNA and siRNA-peptide complex at physiological pH 7.4; lanes 4 and 5 contain siRNA and siRNA-peptide complex at late endosomal pH 5.5; and lane 6 contains siRNA-peptide complex at late endosomal pH 5.5 in the presence of cathepsin B, release of siRNA can be observed. (F) Evaluation of GAPDH silencing in Vero E6 cells using GAPDH siRNA/HE25 complex at various molar ratios, in the presence and absence of 10 nM CA-074-ME, a cathepsin B inhibitor. Error bars indicate mean  $\pm$  SD based on three biological replicates. Data were analyzed using GraphPad Prism, employing a two-way ANOVA and multiple comparison tests ( $^*p < 0.0332$ ;  $^{**}p < 0.0021$ ;  $^{***}p < 0.0002$ ;  $^{****}p < 0.0001$ ) for statistical significance evaluation.

complex colocalizes with ITGAV, together, suggests that the internalization of siRNA/HE25 complex may be triggered by integrin binding. Finally, we tested whether increasing doses of HE25 could inhibit the binding of spike RBD to ACE2, ITGAV, and ITGA2 in a competitive ELISA. Figure 5D demonstrates that escalating doses of HE25 significantly impeded the interaction between the spike RBD and both ACE2 and ITGAV receptors, achieving a 50% reduction in binding within the tested concentration range. However, this inhibitory effect of HE25 was considerably less pronounced on the ITGA2 receptor that did not efficiently bind to HE25. We conclude that HE25 binds and inhibits spike RBD, ACE2, and ITGAV, and our data suggest that the peptide's binding to ITGAV promotes the transportation of siRNA molecules inside the cells.

We further explored the function of Cathepsin B in facilitating the release of siRNA from the HE25 complex within endosomes. This investigation was crucial, given that HE25 was specifically engineered to leverage this mechanism for efficient siRNA delivery. Cathepsin B is involved in SARS-CoV-2 viral coat disassembly and has been proposed as a new potential target for COVID-19 therapy.<sup>43</sup> HE25 peptide is composed of two domains, where the N-terminal domain is negatively charged at physiological pH (pH 7.4) and interacts with a C-terminal positively charged domain.

At the low pH of the late endosome (pH 5.5), the histidines within the N-terminal domain become positively charged and repulse the opposite domain. The conformational change of the peptide unmasks the sequence recognized and cleaved by cathepsin B (sequence: GFLG), allowing the release of the siRNA, as shown by EMSA in which the peptide-siRNA complex was incubated with cathepsin B at pH 5.5 (Figure 5E). In addition, the effectiveness of GAPDH gene silencing in Vero E6 cells treated with GAPDH siRNA/HE25 was notably diminished when exposed to the cathepsin B inhibitor CA-074-ME (Figure 5F). This implies that cathepsin B, within the endosomal environment, plays a crucial role in the degradation of HE25, an essential process for the selective and efficient release of the encapsulated siRNA

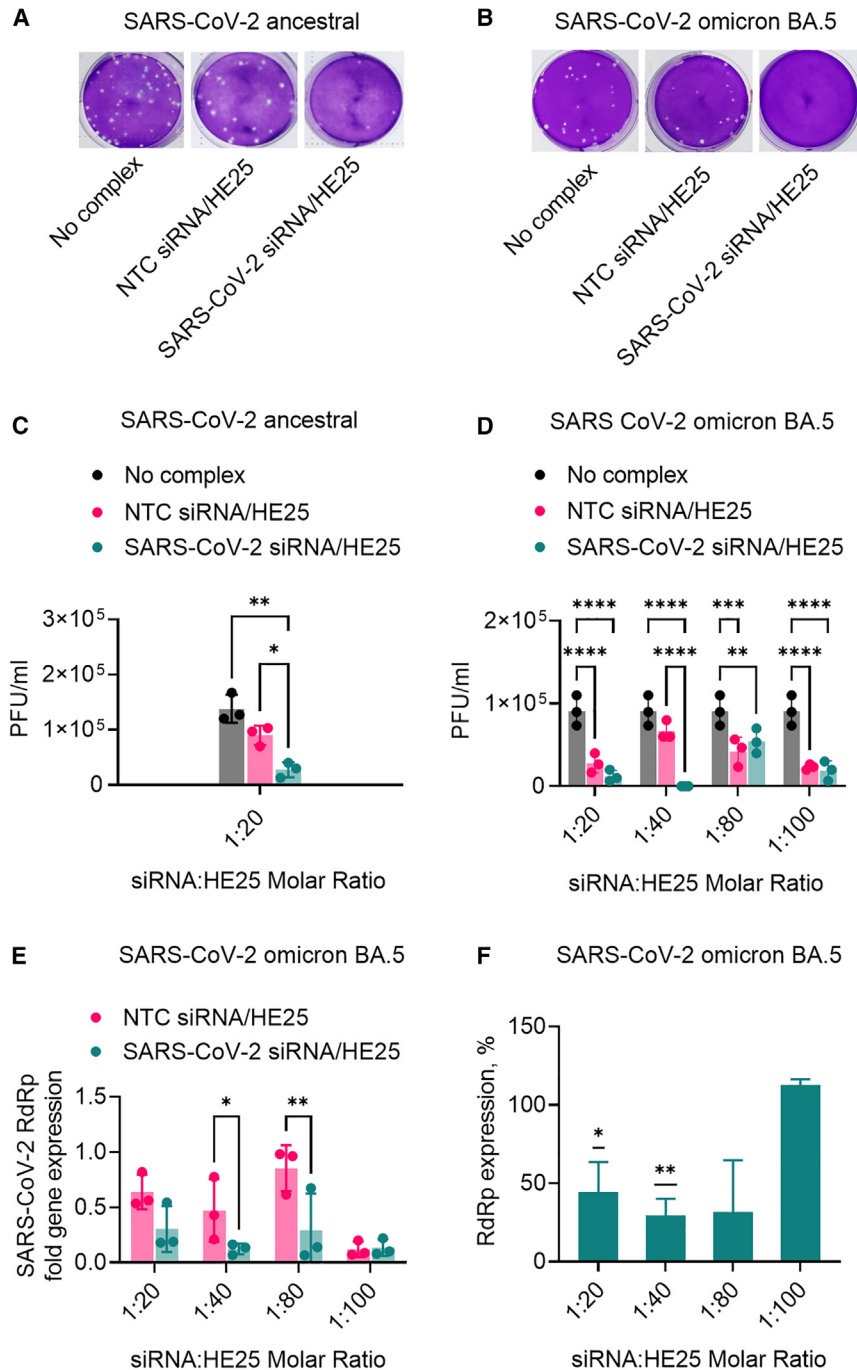


**Figure 6. Inhibition of SARS-CoV-2 replication by siRNA/HE25 complex**

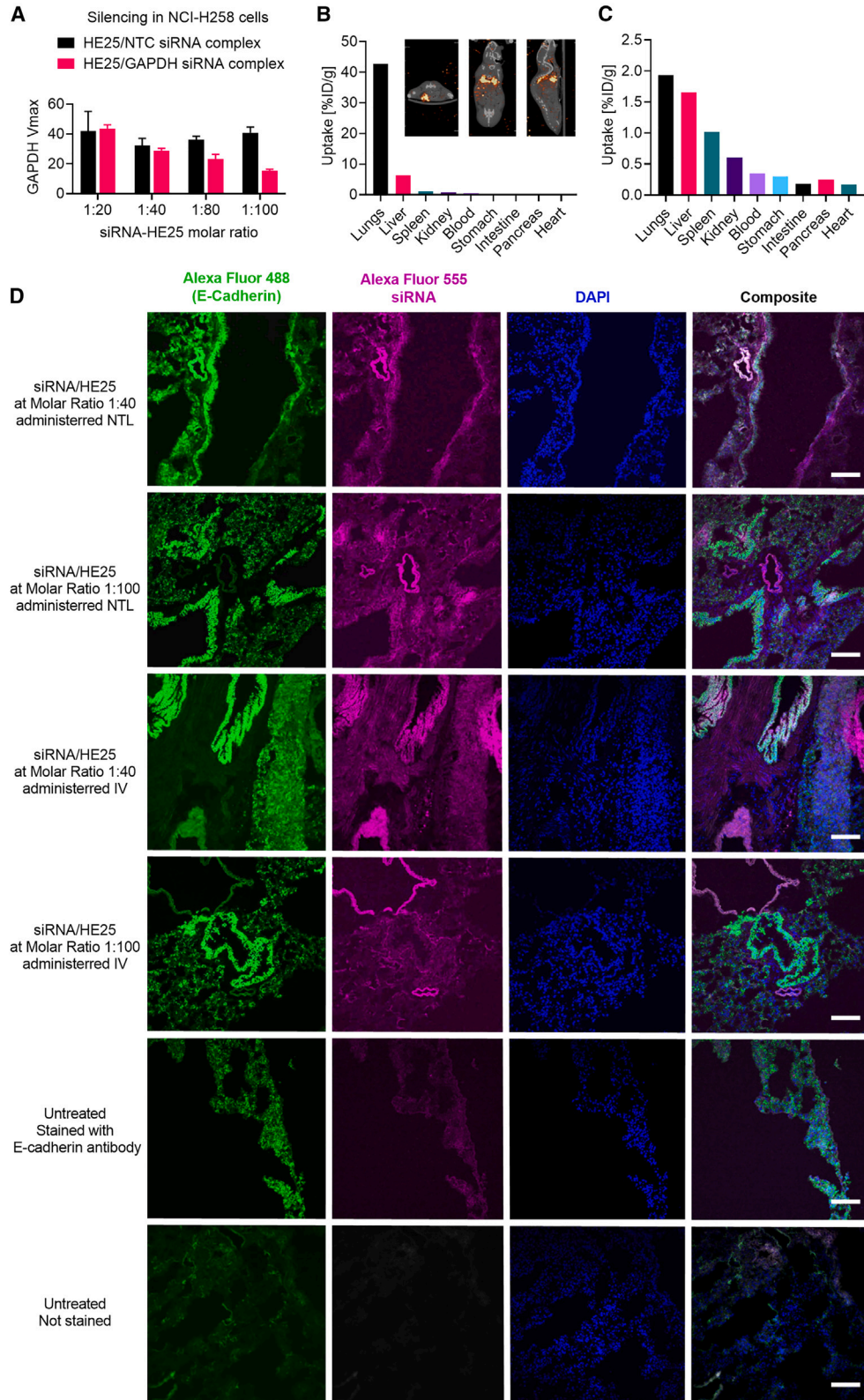
Plaque assay demonstrating reduced SARS-CoV-2 plaque numbers following treatment with NTC-siRNA/HE25 or SARS-CoV-2 siRNA/HE25 complex, conducted on both ancestral SARS-CoV-2 (A and C) and the Omicron subvariant BA.5 (B and D). Results are presented as plaque-forming units (PFU)/mL. (E) and (F) show RdRp expression analyzed by RT-qPCR. Error bars represent mean  $\pm$  SD from three biological replicates. Analysis was performed using GraphPad Prism through one-way or two-way ANOVA, along with multiple comparison tests for statistical significance. In (F), the percent remaining expression was evaluated using a one-sample t test to determine deviation from 100% gene expression. Significance levels are indicated as \* $p < 0.0332$ ; \*\* $p < 0.0021$ ; \*\*\* $p < 0.0002$ ; \*\*\*\* $p < 0.0001$ .

**SARS-CoV-2 siRNA/HE25 complex inhibits SARS-CoV-2 replication up to 100% by combined cell entry blockage and silencing**

Next, we analyzed the capability of the peptide-siRNA complex to inhibit the replication of live, authentic SARS-CoV-2 *in vitro* using the siRNA that targets the SARS-CoV-2 RdRp. Authentic ancestral SARS-CoV-2 or the Omicron subvariant BA.5 of SARS-CoV-2 were added to Vero cells and subsequently incubated with HE25 complexed with either a non-targeting or an SARS-CoV-2 RdRp targeting siRNA (NTC-siRNA/HE25 or SARS-CoV-2 siRNA/HE25). HE-cleav-RGD/SARS-CoV-2 siRNA complexes efficiently blocked ancestral and Omicron BA.5 SARS-CoV-2 replication *in vitro* as determined by a plaque assay (Figures 6A–6D), while NTC-siRNA/HE25 showed partial inhibition of SARS-CoV-2 replication, likely due to the peptides' cell entry-blocking effect as shown in Figure 5D. For the Omicron BA.5 variant, at a molar ratio of 1:20–1:40, the combination of cell entry blockage and silencing resulted in complete inhibition of SARS-CoV-2 replication (90%–100% inhibition), while at molar ratios of 1:80–1:100, the effect of the SARS-CoV-2 targeting siRNA was reduced, and the effect of the NTC/HE25 siRNA was increased (Figure 6D). In fact, at high molar ratios, the receptor binding and blockade might

interfere with complex internalization and gene silencing due to steric hindrance. We hypothesize that at high molar ratio, the HE25 portion of the siRNA/HE25 complex remains attached to the cell surface so that the effect of receptor blockade is increased, while the effect of the RdRp silencing is reduced. Our hypothesis regarding the efficacy of the SARS-CoV-2 siRNA/HE25 complex in silencing the RdRp gene in Vero E6 cells infected with the SARS-CoV-2 Omicron BA.5 variant was

following its internalization into the cells. These results highlight the critical involvement of cathepsin B in the intracellular delivery mechanism of the siRNA/HE25 complex. Furthermore, the presence of histidines leads to a proton sponge effect that destabilizes the endosomal membrane and triggers the release of the endosomal content in the cytosol, allowing the siRNA to reach the target.



(legend on next page)

validated through RT-qPCR analysis (Figures 6E and 6F). The results confirmed that optimal RdRp gene silencing occurred at molar ratios ranging from 1:20 to 1:80. Interestingly, at a 1:100 M ratio, lower RdRp levels were observed in the control group treated with non-targeting siRNA/HE25, suggesting reduced viral internalization under these conditions. To rule out any potential interference from precipitated complex on the SARS-CoV-2 infection in Vero cells, control experiments were conducted with uninfected Vero cells both with and without the siRNA/HE25 complex. The uninfected control layer treated with SARS-CoV-2 siRNA/HE25 complex showed some cell clusters observed as increased crystal violet density in the middle, but no evidence of precipitates, either visually or under microscopic examination (Figure S5).

#### Distinct administration routes of HE25 in CIEA NOG mice: Tail vein injection and nose-to-lung delivery lead to selective pulmonary uptake in endothelial and epithelial structures

In initial studies, we found that GAPDH siRNA/HE25 complex incubated with NCI-H358 lung epithelial cells *in vitro* leads to up to 85% silencing of GAPDH (Figure 7A). This suggested that SARS-CoV-2 siRNA/HE25 complex may efficiently target SARS-CoV-2-infected epithelial cells of the lungs.

To evaluate the *in vivo* biodistribution of HE25, it was labeled with <sup>125</sup>I and administered intravenously alone or in combination with siRNA to CIEA NOG mice by tail vein injection and analyzed using single-photon emission computed tomography/computed tomography (SPECT/CT) scanning 4 h or 24 h after administration. Animals were euthanized after 24 h, their organs excised, and radioactivity of the individual organs measured (Figures 7B and 7C). SPECT/CT scans and *ex vivo* biodistribution analysis revealed that HE25 peptide accumulated in the lungs, exhibiting a 7- and 40-fold higher uptake than liver and blood, respectively, 24 h after administration. At a molar ratio of 1:100, the lung accumulation of the siRNA/HE25 complex decreased by a factor of 20. Notably, even with this significant decrease, the complex's accumulation in the lungs was markedly higher compared with all other organs.

Next, Alexa Fluor 555-tagged siRNA/HE25 complex was administered via intravenous (i.v.) injection and nose-to-lung delivery to mice at molar ratios of 1:100 and 1:40, and their accumulation within lung structures were analyzed 24 h post-administration (Figure 7D). Utilizing immunohistochemistry and confocal microscopy imaging, we observed distinct patterns of accumulation based on the adminis-

tration route. Specifically, following i.v. injection, there was notable accumulation in the endothelium of veins and arteries. In contrast, with nose-to-lung delivery, we observed accumulation predominantly in the epithelium of bronchi and bronchioles with the Alexa Fluor-tagged siRNA/HE25 complex.

To achieve comprehensive coverage of all lung structures, a combined approach utilizing both nose-to-lung and i.v. injection routes may be an effective strategy. This dual-route administration could potentially enhance the distribution and efficacy of the HE25 complex throughout the various pulmonary compartments, thereby maximizing its therapeutic impact.

#### SARS-CoV-2 siRNA/HE25 complex demonstrates no adverse effects in Balb/c mice across multiple administration routes

To investigate the biosafety of the SARS-CoV-2 siRNA/HE25 complex, Balb/c mice underwent biweekly treatments for 2 weeks, receiving the complex through either nose-to-lung delivery or i.v. injection. Control mice receiving just the vehicle, phosphate-buffered saline (PBS), administered via the same routes, were included. At the tested dose of 0.2 mg/kg, no acute toxicity was observed for either administration route. To evaluate long-term toxicity, we monitored the health impact on the mice by tracking weight changes every 5 days, but no weight loss was observed (Figures 8A and 8B). At day 15, the mice were euthanized and excised lung tissue was analyzed. Sectioning of the lung tissues and staining with Masson trichrome, a method specifically employed to detect fibrosis, revealed no sign of increased fibrosis in the group receiving the SARS-CoV-2 siRNA/HE25 complex (Figures 8C–8E). Based on these studies, we find no indications that the administration of the siRNA/HE25 complex negatively impacts the overall health of the mice or induces significant fibrotic changes in their lungs. Together, these results indicate that our SARS-CoV-2 siRNA/HE25 complex may be a promising novel therapeutic for severe COVID-19 infection.

#### DISCUSSION

Although effective vaccines have been developed against SARS-CoV-2, not all individuals are vaccinated and others, particularly immunosuppressed individuals, do not respond to these vaccines. Therefore, there remains a need for specific and effective SARS-CoV-2 therapeutics to relieve symptoms in patients hospitalized due to COVID-19.

A promising approach for the treatment of severe COVID-19 disease is silencing the viral mRNA by administering an siRNA against

#### Figure 7. Gene silencing in lung cells, biodistribution, and compartmental analysis of siRNA/HE25 complex

(A) Silencing of GAPDH in NCI-H358 lung epithelial cells from bronchioalveolar carcinoma by GAPDH siRNA/HE25 complex, with error bars showing mean  $\pm$  SD of three biological replicates. (B) SPECT/CT scan of mice 4 h post-administration and *ex vivo* biodistribution 24 h after administration of <sup>125</sup>I-labeled HE25 peptide. (C) Uptake of siRNA/<sup>125</sup>I-labeled HE25 peptide complex; uptake of free <sup>125</sup>I in the thyroid is excluded from the graph. (D) Confocal immunofluorescence microscopy of mouse lungs treated with Alexa Fluor 555-tagged siRNA/HE25 complex (magenta pseudocolor), administered via nose-to-lung (first and second rows) or i.v. injection (third and fourth rows). Lung structures have been labeled with Alexa Fluor 350 by E-Cadherin immunostaining (green pseudocolor). Areas of colocalization between green and magenta are depicted in white, signifying the spatial interaction between the siRNA/HE25 complex and lung structures. Pseudocolors were selected to enhance accessibility for individuals with color vision deficiencies. DAPI staining is shown in blue. The scale bar in the lower right corner of the composite panels represents 100  $\mu$ m. Data were analyzed using GraphPad Prism with a two-way ANOVA and multiple comparisons test ( $^*p < 0.0332$ ;  $^{**}p < 0.0021$ ;  $^{***}p < 0.0002$ ;  $^{****}p < 0.0001$ ) for statistical significance.

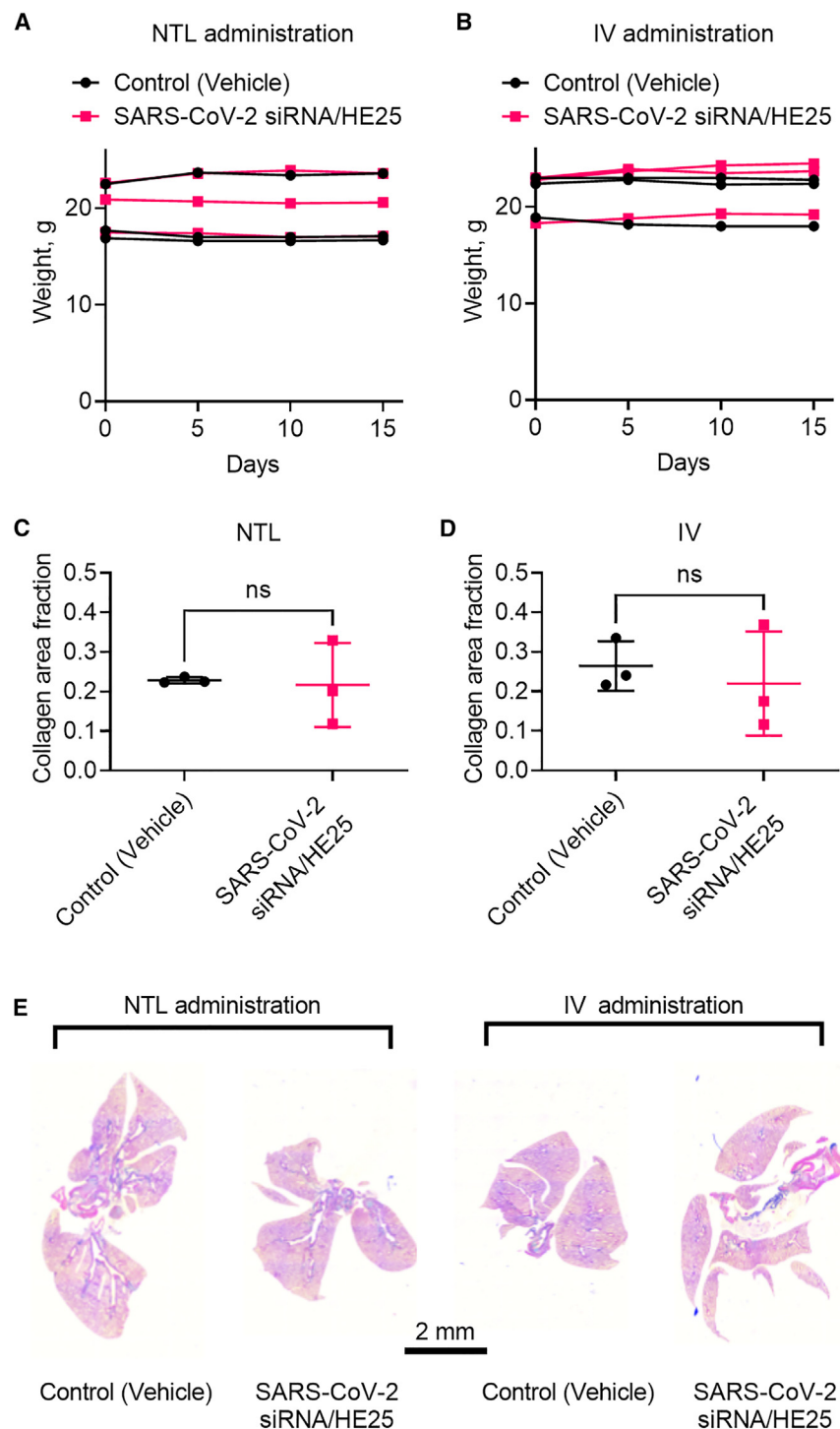


**Figure 8. Assessment of body weight and lung fibrosis in BALB/c mice following nose-to-lung and i.v. administration of SARS-CoV-2 siRNA/HE25 complex**

Weight tracking of BALB/c mice following nose-to-lung administration (A) or i.v. injection (B) with SARS-CoV-2 siRNA/HE25 complex, performed biweekly over 15 days. Quantitative assessment of lung fibrosis is conducted using Masson's trichrome staining on excised lung tissues from mice treated via nose-to-lung (C) or i.v. injection (D). Error bars indicate mean  $\pm$  SD from three biological replicates. (E) displays corresponding Masson's trichrome-stained lung tissue micrographs. Statistical analysis was conducted using GraphPad Prism with two-tailed unpaired t test ( $*p < 0.0332$ ;  $**p < 0.0021$ ;  $***p < 0.0002$ ;  $****p < 0.0001$ ) to determine statistical significance.

vehicles that can be designed to allow spontaneous siRNA encapsulation and specific receptor binding.<sup>46,47</sup>

The study presents HE25, a peptide featuring an RGD sequence and a DMBT1-derived siRNA binding domain (VRVLXXXXW) that enable it to spontaneously encapsulate siRNA, which sets it apart from other RGD peptides that generally need covalent linkage to oligonucleotides.<sup>38</sup> HE25's higher siRNA encapsulation efficiency is linked to its self-assembling amino-terminal (HEHHEHHEHEH) and carboxy-terminal (RVRVLRGDKW) sequences, an approach previously employed in pH-responsive peptides.<sup>48</sup> HE25 shows effective siRNA encapsulation utilizing self-assembling, cell-penetrating peptide mechanisms involving tryptophans and arginines. It employs electrostatic, hydrophobic, and hydrogen bonding interactions and is influenced by temperature and pH, indicating conformational flexibility.<sup>49,50</sup>

The characterization of the SARS-CoV-2 siRNA/HE25 complex highlighted several advantages. Other studies have established that a 100-nm diameter for complexes is optimal for enhancing cellular uptake and ensuring biological stability. This size range effectively balances the need for efficient cellular entry while maintaining the complex's structural

RdRp.<sup>9,10,16</sup> However, due to their limited blood stability and intracellular bioavailability, siRNA molecules must be combined with a vehicle. Although multiple delivery systems can be employed for siRNA administration, a limited number of vehicles can be designed to target specific receptors.<sup>44,45</sup> Cell-penetrating peptides are flexible

integrity in a biological environment.<sup>51</sup> The positive charge enhances cellular interactions, crucial for siRNA delivery.<sup>52</sup> The rounded morphology, a trait of effective drug carriers, aids in cellular entry.<sup>53</sup> The resolution of stability issues in ultrapure water by adding 1% PEG2000 is consistent with existing data indicating

that steric hindrance stabilizers can enhance nanoparticle stock stability.<sup>54</sup>

The demonstrated stability of the siRNA/HE25 complex in various biological serums, including FBS, mice, and humans, coupled with its silencing efficiency, paves the way for its potential translational application. This advancement suggests promising prospects for clinical use, where stability and efficiency in complex biological environments are crucial for therapeutic success.

HE25, initially designed to target integrins, also binds to receptors such as ACE2 and neuropilin-1, involved in SARS-CoV-2 entry. Its addition disrupts the spike-ACE2 and ITGAV interaction, suggesting HE25 could block virus entry by competing for receptor binding. Additionally, in Vero E6 cells, Alexa Fluor 555 siRNA/HE25 was found in the endosomal compartment similar to other RGD peptides that undergo receptor-mediated endocytosis.<sup>55</sup> However, the siRNA release and endosomal escape are common issues of nanoparticles and cell-penetrating peptides,<sup>56,57</sup> while GAPDH siRNA/HE25 complex achieved effective GAPDH silencing, showing HE25's role in siRNA transfection. To facilitate the disassembly of the peptide-siRNA complex and the siRNA release in the endosomal environment, we inserted the sequence GFLG in HE25 that is specifically cleaved by the endosomal cathepsin B, an approach employed in the design of prodrugs.<sup>58</sup> Furthermore, multiple histidine residues were included in the sequence to enhance the endosomal escape by the proton sponge effect, as reported for other cell-penetrating peptides.<sup>48,59</sup>

Until now, RGD-containing peptides have been reported to possess either receptor inhibition or oligonucleotide transport capabilities.<sup>60</sup> In contrast, our results indicate that HE25 exhibits both of these abilities. This novel study reveals that HE25 uniquely inhibits SARS-CoV-2, acting as a cell entry inhibitor without directly targeting viral genes. When used alongside RdRp-targeting siRNA, the inhibition is notably enhanced, indicating a cooperative effect between mechanisms that block virus entry and silence the viral RNA polymerase. The partial inhibition of SARS-CoV-2 by NTC-siRNA/HE25 confirms that HE25 functions as a cell entry inhibitor for the virus, as no siRNA targeting a viral gene was utilized. Furthermore, when combined with RdRp-targeting SARS-CoV-2 siRNA, the inhibition efficiency was enhanced, suggesting a synergistic effect between the inhibition of virus cell entry and the silencing of the viral RNA-dependent RNA polymerase. RT-qPCR confirmed the silencing occurs mainly at molar ratios 1:20–1:80, while at molar ratio 1:100 we observed low RdRp in samples treated with non-targeting control related with low virus amount, and no difference with samples treated with SARS-CoV-2 siRNA/HE25.

Integrin-targeting RGD peptides and CendR peptides, which target NRP-1, have been known to exhibit lung tropism.<sup>61,62</sup>

HE25 showed notable lung accumulation in mice, as observed in SPECT/CT scans with 125I-labeled HE25 and its siRNA complex,

and in those administered Alexa Fluor 555 siRNA/HE25 via i.v. or nose-to-lung routes, targeting lung endothelial or epithelial structures. This notable affinity of HE25 to the lungs can be attributed to the high expression levels of integrins and NRP-1 receptors in the respiratory tract, which HE25 was shown to target. Furthermore, ACE2, targeted by HE25, is abundantly expressed in lung tissue. Its age-related increase correlates with higher susceptibility and severity of COVID-19 infections.<sup>27</sup> The SARS-CoV-2 siRNA/HE25 complex caused no acute toxicity, weight change, or significant lung fibrosis in mice, suggesting a low-toxicity alternative for lung targeting.<sup>63</sup>

With evolving data on SARS-CoV-2 and its variants, the number of investigated drugs is growing, but currently, none target the virus using multiple complementary methods.<sup>64</sup> Multitargeted drugs offer benefits over combination therapy, including simpler regimens, predictable pharmacokinetics and dynamics, potentially less toxicity, and increased efficacy.<sup>65</sup> The siRNA in this study targets a conserved domain of the RdRp protein, stable across SARS-CoV-2 variants, potentially making the complex effective against new and emerging variants.

In summary, the HE25 peptide complex with SARS-CoV-2 RdRp-targeting siRNA shows promise in inhibiting virus replication, suggesting potential as a COVID-19 therapy. Given the likelihood of future pandemics, developing such adaptable anti-viral strategies is crucial. While our siRNA delivery method may need refinement for new pathogens, it could be quickly adapted for future outbreaks. Further tests are needed to assess its *in vivo* effectiveness against SARS-CoV-2, first in animals and then in humans.

## MATERIALS AND METHODS

### *In silico* studies

The structure of peptide HE25 was predicted using AlphaFold, employing its advanced deep learning algorithms for accurate protein structure prediction.<sup>66</sup> The siRNA molecule, obtained from the Protein DataBank (PDB) database (entry code 2F8S), was used in conjunction with the predicted structure of HE25 for RNA-peptide docking simulations, conducted using HDock.<sup>67</sup> This approach combines template-based modeling and *ab initio* docking to explore potential interactions. The resulting RNA-peptide complex conformations, suggested by HDock based on binding affinity and geometric complementarity, were visualized and analyzed using UCSF Chimera.<sup>68</sup> This facilitated a comprehensive examination of the RNA-peptide binding sites and the overall structural arrangement of the complex.

### Custom-produced peptides and siRNAs

The HE25 peptide was synthesized by GenScript's custom synthesis service. The supplied lyophilized peptide had a purity exceeding 98% and a peptide content of 50.82%, as determined by nitrogen analysis. Trifluoroacetic acid (TFA) removal was not performed, as preliminary experiments indicated that replacing the counter ion adversely affected the peptide's activity. The endotoxin level was maintained at  $\leq 0.01$  EU/ $\mu$ g. For reconstitution, HE25 was dissolved

in ultrapure water with 1% DMSO to achieve a final stock concentration ranging from 0.5 to 1 mM. Additionally, the SARS-CoV-2 RdRp-targeting siRNA, previously optimized by Musa Khaitov et al. (sense: Ggaaggaaguucuguugaa+T+Tt; antisense: uucaacagaacuuccuucc+T+Tt), was also synthesized by GenScript.<sup>17</sup> This siRNA was supplied lyophilized, achieving a purity of 99%, and was resuspended in ultrapure water to a final concentration of 100  $\mu$ M in the stock solution.

### Cell lines

The original Vero E6 cell line was obtained from the American Type Culture Collection (ATCC), and NCI-H358 cell line from ATCC was kindly provided by Prof. Brage Storstein Andresen and Dr. Caroline Alqvist Lindegaard from the Department of Biochemistry and Molecular Biology of the University of Southern Denmark. Vero E6 and NCI-H358 were routinely propagated in Dulbecco's Modified Eagle's Medium (DMEM) with GlutaMax (Gibco) supplemented with 5% FBS; Sigma-Aldrich). Cells were grown in a humidified atmosphere of 5% CO<sub>2</sub> at 37°C.

### Viruses

SARS-CoV-2 virus stocks of ancestral SARS-CoV-2 or SARS-CoV-2 omicron BA.5 were isolated in-house by culturing oropharyngeal swabs from COVID-19 tests. After identifying the strain by sequencing, the swab was cultured in Vero E6 cells for three passages, then centrifuged at 450  $\times$  g for 5 min to remove cell debris and frozen at -80°C.

### Animal models

NOG CIEA and Balb/c mice were obtained by Taconics and were approximately 7 weeks old and weighed 20 g. All animal experiments were approved by the Experimental Animal Committee of The Danish Ministry of Justice and were performed at the animal core facility at the University of Southern Denmark. Mice were housed under pathogen-free conditions with *ad libitum* food and water. The light/dark cycle was 12 h light/dark, with lights turned on from 6 a.m. to 6 p.m. Housing temperature was 21  $\pm$  1°C and relative humidity 40%–60%.

### EMSA

HE25 was dissolved in 1% DMSO in ultrapure RNase-free water at 0.5 mM. Stealth RNAi siRNA Negative Control siRNA (10  $\mu$ M) was diluted to 0.5  $\mu$ M with Ultrapure RNase-free water, and 10  $\mu$ L of siRNA solution was added with 10  $\mu$ L of peptide solution with concentrations ranging from 10  $\mu$ M to 100  $\mu$ M, corresponding to molar ratios 1:20–1:100. Peptide-siRNA solutions were incubated for 1 h at 4, 25, 37 or 50°C to encapsulate. Citric acid was employed to obtain pH 4 in the low pH experiments. In the case of EMSA competition assays, siRNA/HE25 complex was prepared similarly, then added with 2  $\mu$ L of 100 mg/mL DSS, or 8 M urea or 20% NaCl before or after encapsulation. Preformed solutions of the peptide-siRNA complexes were mixed with dye-free gel-loading buffer (glycerol at 5% final concentration) and exposed to electrophoresis on agarose gel (4% [w/v]) stained with ethidium bromide. FastRuler UltraLow Range DNA Ladder (ThermoFisher SM1233) was employed as a ladder. MOPS buffer

at pH 7.5 was used as a running buffer to maintain physiological pH during the electrophoresis; in the case of low pH encapsulated complex, MOPS buffer pH was lowered to 5.5. Electrophoresis was performed at 70 V for 30 min, and thereafter the gel was imaged by exposure to UV light. To investigate Cathepsin B-mediated siRNA release, NTC5/HE25 siRNA was prepared at 1:100 M ratio and 1  $\mu$ M siRNA according to the above protocol, in a total volume of 10  $\mu$ L. Subsequently, complexes were incubated for 30 min at 37°C with 1  $\mu$ L cathepsin B stock solution dissolved in 45  $\mu$ L of MES buffer (0.15 M, pH 5) to mimic the late endosomal environment. Thereafter, electrophoresis on agarose gel was performed according to the above protocol.

### Nano tracking analysis and zeta potential measurement

Particle size, concentration, and zeta potential were measured using ZetaView Nanoparticle Tracking Analyzer PMX-220 (Particle Metrix, Germany). SARS-CoV-2/HE25 samples at molar ratios 1:20, 1:40, 1:80, 1:100, and 1:200 were prepared in ultrapure water as described above and diluted in freshly ultrapure water to a final volume of 1 mL. The ideal dilution factor was found by aiming for 140–200 particles/frame. The particles were measured using 10 cell positions, with the following capture settings: cell temperature: 23°C–25°C, sequence length: 30, frame rate (fps): 30, switch frame: 10, video resolution: medium, laser wavelength (nm): 488, sensitivity: 60–80, shutter: 100–200, and following analysis settings: min size (nm): 1.0, max size (nm): 1000, trace length: 12, tracking radius: 3 px. All measurements were performed for three separate stocks and done in triplicates for size, and in duplicates for zeta potential, by injecting 100  $\mu$ L fresh sample before the next measurement. The data were collected using the ZetaView software, PEX.

### Transmission electron microscopy

SARS-CoV-2/HE25 samples were prepared at molar ratios of 1:20, 1:40, 1:80, 1:100, and 1:200 in ultrapure water as previously described and 5  $\mu$ L of the complex suspension were pipetted on a copper mesh grid and incubated for 30 min at room temperature. The suspension was then removed and the adsorbed particles were fixed with 4% formaldehyde and 1% glutaraldehyde for 5 min. Fixation was followed by washes with water and incubation for 20 min with 3% uranyl acetate as a contrast agent. Samples were imaged using a JEM-1400 Plus transmission electron microscope, equipped with Quemsas TEM CCD camera.

### Serum stability assays

The kinetic stability assay of the FRET-siRNA/HE25 complexes in sera was conducted using specifically prepared complexes at molar ratios of 1:20, 1:40, 1:80, 1:100, and 1:200. These complexes were formulated in 60  $\mu$ L of ultrapure water following the above-described protocol. Subsequently, 20  $\mu$ L aliquots of each complex were dispensed into triplicate wells of a black-walled 96-well plate, each containing 80  $\mu$ L of FBS, normal mouse serum (Invitrogen, product code 10410), or serum from a healthy human donor at final concentration of 2.5%. Fluorescence readings were taken every 10 min for 1 h using an i3X SpectraMax (Molecular Devices) plate reader. The excitation

and detection parameters were set at 465 nm for excitation, with fluorescence emission detected at 520 nm for FAM detection domain and 600 nm for TAMRA detection. To account for background interference in the analysis, control wells containing only 2.5% serum were used to acquire baseline fluorescence signals. These background readings were then subtracted from the experimental data, ensuring that the results reflected only the specific fluorescence emitted by the siRNA/HE25 complexes, free from any serum-induced artifacts. Signal acquisition was facilitated by SoftMax Pro Software (Molecular Devices).

For the FRET-EMSA stability assay, FRET-siRNA/HE25 complex was prepared at a molar ratio of 1:100 according to the protocol described for the classical EMSA. Next, FRET-siRNA/HE25 complex was treated with 2.5% FBS diluted in PBS and incubated for 30 min at 37°C after which 28 µg/µL of proteinase K was added to inhibit the serum RNases. The FRET-siRNA/HE25 complex was treated with DSS (2.8 mg/mL), urea (0.22 mg/mL), and SDS (0.28%) to disassemble the complex and release the FRET-siRNA. The samples containing FBS-treated or untreated FRET-siRNA and FBS-treated or untreated, assembled or disassembled FRET-siRNA/HE25 complex were added with dye-free loading buffer (glycerol at 5% final concentration) and exposed to electrophoresis on agarose gel (4% [w/v]) without staining. The electrophoresis was performed in the same conditions as described for EMSA. The gel was imaged with a Spectrum In Vivo Imaging System (IVIS, PerkinElmer) by excitation at 465 nm, detection at 520 nm for FAM and 600 nm for TAMRA, and 15s exposure time.

#### Transfection of Vero E6 and NCI-H358 cells with siRNA/HE25 complex

GAPDH siRNA/HE25 complex at different molar ratios and concentrations was prepared as described above. GAPDH silencing experiments were performed as reverse transfections using 96-well plates. HE25 was complexed with GAPDH (Ambion Silencer Select GAPDH siRNA) or non-targeting siRNA (NTC-siRNA, Silencer Select Negative Control No. 1 siRNA, ThermoFisher). For each well, the peptide-siRNA complexes were prepared in RNase-free ultrapure water in 10 µL, then diluted with 40 µL of serum-free Opti-MEM (Gibco). Vero E6 or NCI-H358 cells were resuspended in DMEM supplemented with 5% FBS in 50 µL and mixed with the peptide-siRNA mixture directly on the 96-well plate. For both cell lines, the number of cells seeded was  $1 \times 10^4$  cells/well. Plates were placed in the cell incubator for 3 days and then analyzed with KDalert GAPDH Assay Kit according to the manufacturer's instructions. For each experiment, two technical replicates and three biological replicates were included. The biological replicates were generated by cultivating each cell line in three T25 flasks.

To analyze the endocytosis pathway, the silencing of GAPDH was performed by administering GAPDH siRNA/HE25 complex at different molar ratios at a final siRNA concentration of 50 nM, according to the protocol described above. The endocytosis inhibitors, chlorpromazine (28 µM), dynasore (80 µg/mL), nystatin (26 µg/mL), or orcyto-

chalasin D (2 µM), were added to DMEM supplemented with 5% FBS and added to the plate before the GAPDH siRNA/HE25 complex, according to the previous reported protocol.<sup>69</sup> The expression of GAPDH was measured using the KDalert GAPDH Assay Kit according to the manufacturer's instructions. For each experiment, two technical replicates and three biological replicates were included. The biological replicates were generated by cultivating each cell line in three T25 flasks.

#### Authentic SARS-CoV-2 inhibition experiments

SARS-CoV-2 inhibition experiments were performed in six-well plates. HE25 was complexed with SARS-CoV-2 RdRp-targeting or with NTC5 siRNA. For each well, the peptide-siRNA complexes were prepared in RNase-free ultrapure water in 200 µL, then diluted with 800 µL of serum-free Opti-MEM (Gibco). Vero E6 cells were resuspended in DMEM supplemented with 5% FBS in 1,000 µL/well and added to the peptide-siRNA mixture directly on the six-well plate at a seeding density of  $5 \times 10^5$  cells/well for a final siRNA concentration of 50 µM. Plates were placed in the cell incubator for 1 day and then infected with ancestral SARS-CoV-2 or Omicron subvariant BA.5 of SARS-CoV-2 according to a plaque assay protocol previously described.<sup>70</sup> After removing the medium containing the complex, each well was treated with 300 µL of the SARS-CoV-2 virus solution prepared in DMEM supplemented with 2% FBS and placed in the cell incubator for 1 h. Thereafter, each well was layered with 0.75% agarose gel prepared in DMEM supplemented with 2% FBS (final concentration) and placed in the cell incubator for 48 h (ancestral SARS-CoV-2) or 72 h (Omicron subvariant BA.5 of SARS-CoV-2). Subsequently, the plates were processed in distinct manners tailored to the specific requirements of each ensuing assay, as detailed below.

For the plaque assay, cells were fixed with 800 µL/well 10% formalin for 1 h at room temperature. Subsequently, the formalin was removed and the agarose gel was lifted from the wells. The bottom of the wells was stained with 10% crystal violet solution for 2 min and washed before being imaged.

For the RT-qPCR experiments, the agarose layer and the virus-containing medium were removed and wells were washed with PBS. Cells were lysed using the ISOL reagent, and RNA was extracted through a protocol that integrates organic solvent treatment with affinity chromatography. RT-qPCR was conducted using the COVID-19 TaqMan RT-PCR Kit (Norgen Biotek, TM67240), following the manufacturer's protocol.

#### Immunofluorescence assays

For the experiments *in vitro*, Vero E6 cells ( $1 \times 10^3$  cells/chamber) were transfected with BLOCK-iT Alexa Fluor Red Fluorescent Control (Invitrogen, 14750100) complexed with HE25 at molar ratios 1:20, 1:40, 1:80, and 1:100 in Nunc Lab-Tek II Chambered Coverglass (ThermoScientific 155360) according to the protocol described above. After 24 h, cells were stained with HCS CellMask staining solution (Invitrogen, H32721) according to manufacturer's instructions, and subsequently fixed with 10% formalin, blocked and permeabilized

with 0.2% Triton X-100 in 10% normal donkey serum/PBS. Samples were incubated with the following primary antibodies at 4°C overnight: ITGAV (Abcam, ab11470-50, 1:100), Rab4 (Thermo Scientific, PA3912, 1:250), Rab9 (Thermo Scientific, MA3067, 1:250), and Rab11A (Thermo Scientific, 715300, 1:250). Subsequently, cells were washed with PBS and treated with corresponding secondary antibodies (goat-anti-mouse or goat-anti-rabbit Alexa Fluor 350, Thermo Scientific, 1:1,000), for 1 h at room temperature, washed with PBS and mounted with ProLong Gold Antifade Mountant (Thermo Scientific, P36930). Samples were imaged using a Nikon AX MP multi photon confocal microscope equipped with NSPARC (Nikon Spatial Array Confocal detector) confocal multiphoton laser scanning microscope, and with a  $\times 20$ , 0.95 objective. Pictures were analyzed by using FIJI ImageJ (NIH) colocalization JaCoP colocalization plugin.<sup>71,72</sup>

In the *in vivo* experiments, NOG CIEA mice were administered either i.v. or via nose-to-lung delivery with BLOCK-iT Alexa Fluor Red Fluorescent Control (Invitrogen, 14750100) complexed with HE25. The dosing was standardized at 1 mg/kg, and the complexes were prepared at molar ratios of 1:40 or 1:100, following the previously described preparation protocol. After 24 h, mice were anesthetized and subjected to cardiac perfusion with PBS from the small circulation. Lung lobes were excised and embedded in TissueTeck, then frozen in dry ice-cold Isopentane. Cryosection of the lobes were fixed with 10% formalin, permeabilized with 0.1% Triton X-100 in PBS, and blocked with 3% BSA. Sections were incubated with E-cadherin antibody (Cell Signaling, 3195, 1:500) at room temperature for 2 h. Subsequently, cells were washed with PBS and incubated with goat-anti-rabbit Alexa Fluor 488 (Thermo Scientific, 1:500) for 1 h at room temperature, washed with PBS and mounted with antifade mountant containing DAPI. Samples were imaged using an FV1000MPE Olympus confocal multiphoton laser scanning microscope, equipped with a  $\times 20$  numerical aperture (NA) 0.96 objective.

#### Enzyme-linked immunosorbent assay

Direct ELISA was performed to evaluate the interaction between spike or HE25 and cell receptors. Ninety-six-well plates (Nunc MaxiSorp, ThermoFisher) were coated with HE25 (5  $\mu\text{g}/\text{mL}$ ) or spike RBD (2  $\mu\text{g}/\text{mL}$ ) diluted in carbonate/bicarbonate buffer at 4°C overnight, then washed with PBS-Tween 0.05%. Thereafter, plates were blocked with 1% BSA in PBS for 1 h at room temperature and treated with increasing amounts of recombinant His-tagged ACE2, ITGAV, ITGA5, ITGA2, ITG2B, or NRP1, myc-tagged ITGB3, untagged FIB, or SARS-CoV-2 spike RBD diluted in PBS and incubated for 2 h at room temperature. To ensure accurate background correction, uncoated wells without HE25 were first blocked and then treated with varying concentrations of recombinant proteins and corresponding antibodies. This step was conducted to establish distinct background levels for each recombinant protein concentration. These background readings were subsequently subtracted from the signals obtained in the wells containing HE25, allowing for precise isolation of the specific response attributable to HE25. Subsequently, plates were washed with PBS-Tween 0.05% and treated with Myc-tag, His-tag antibody,

biotinylated anti-FIB (1:1,000 diluted from stock in blocking buffer), or spike RBD antibody depending on the protein and incubated at 4°C overnight. After 12 h, plates were washed with PBS-Tween 0.05% DAKO HRP goat-anti-rabbit or HRP rabbit-anti-mouse secondary antibody (1:1,000 in blocking buffer) or HRP-avidin for 1 h at room temperature. Finally, plates were washed with PBS-Tween 0.05% and treated with ELISA horseradish peroxidase (HRP) reagent (ThermoFisher) for 15 min at room temperature on a shaker. Absorbance was read at 450 nm using a SpectraMax i3x (Molecular Devices).

Competitive ELISA was performed to evaluate the inhibition of spike-cell receptor interaction by HE25. Plates were coated with spike RBD protein in carbonate/bicarbonate buffer at 2  $\mu\text{g}/\text{mL}$  at 4°C overnight. After 12 h, plates were washed with PBS-Tween 0.05% and blocked with 1% BSA in PBS for 1 h at room temperature. Meanwhile, increasing concentrations of HE25 were pre-incubated with ACE2 (0.1  $\mu\text{g}/\text{mL}$ ), ITGAV (4  $\mu\text{g}/\text{mL}$ ), or ITGA2 (0.9  $\mu\text{g}/\text{mL}$ ) in PBS for 1 h at room temperature before being added to the plate and incubated for 2 h at room temperature. Plates were washed with PBS-Tween 0.05% and treated with His-tag antibody (1:1,000 in 2% BSA in PBS) or anti-spike antibody (undiluted) and incubated at 4°C overnight. After 12 h, plates were washed with PBS-Tween 0.05% and incubated with HRP goat anti-rabbit or rabbit anti-mouse antibody at 1:1,000 in blocking buffer for 1 h at room temperature. Finally, plates were washed with PBS-Tween 0.05% and treated with ELISA HRP reagent (ThermoFisher) for 15 min at room temperature on a shaker. Absorbance was read at 450 nm using a SpectraMax i3x (Molecular Devices).

#### Biodistribution experiments

HE25 was labeled with  $^{125}\text{I}$  by histidine iodination according to the following procedure: HE25 peptide (50  $\mu\text{L}$ , 1  $\mu\text{g}/\mu\text{L}$ , PBS buffer pH 8.5), PBS buffer (100  $\mu\text{L}$ , 0.1 M, pH 8.5) and  $^{125}\text{I}$  solution (non-carrier added, 100  $\mu\text{L}$ , 22.5 MBq, diluted with PBS buffer pH 8.5) was mixed in an HPLC vial coated with iodogen (50  $\mu\text{g}$ ) prior to labeling. The mixture was reacted for 60 min and agitated every 10 min. The labeling mixture was transferred from the iodogen tube to an Eppendorf vial. Subsequently, the iodogen tube was washed with  $2 \times 100 \mu\text{L}$  milliQ water, which was added to the labeling mixture. The resulting mixture was either loaded onto a Sep-pak C18 plus cartridge (conditioned using 10 mL ethanol and 10 mL milliQ water), washed with milliQ water, and eluted using 20% TFA solution (0.1% TFA) in MeCN (3 mL) or purified using HPLC (Jupiter 300  $\text{\AA}$ ,  $15 \times 4.7 \text{ mm}$ , 5  $\mu\text{M}$ , gradient of MeCN [A] and 0.1% TFA and milliQ [B]; 0–2 min: 20% A in B; 2–6 min: 20% to 60% A in B; 6–7 min: 60% to 97% A in B; 7–10 min 97% A in B) collecting the product at 9–10 min. Fractions were evaporated using nitrogen flow overnight.

$^{125}\text{I}$ -HE25 or NTC5 siRNA/ $^{125}\text{I}$  HE25 complex at 1:100 siRNA:peptide molar ratio was initially prepared in sterile ultrapure water incubated 1 h at 50°C to allow siRNA encapsulation. Then the solution osmolarity was adjusted to physiological with 5% glucose at the final concentration. Mice were i.v. injected into the tail vein with 160  $\mu\text{L}$

of peptide or peptide-siRNA complex. The total injected peptide mass was adjusted to 2 nmol/mouse with an injected activity of  $66 \pm 0.21$  kBq. At 4 h post injection, the mice were anesthetized with a mixture of 2% isoflurane and 100% oxygen and whole-body SPECT/CT scans were performed using a Siemens Inveon preclinical scanner (Siemens Healthcare, Knoxville, TN, USA) with SPECT acquisition time of 60 min, with the following settings: mouse whole-body collimators, ROR 35, 1.0 rev. and 60 projections per revolution. The CT scans were performed with two bed positions, 270 projections in  $360^\circ$  rotations, bin 4, 80 kV, 500  $\mu$ A, and exposure time of 350 ms. CT and SPECT images were co-registered and the SPECT data were reconstructed using an MAP3D algorithm. After the SPECT/CT scan, all mice were awakened from anesthesia and allowed to roam freely in cages with unrestricted access to food and water. Twenty-four hours later the mice were euthanized by cervical dislocation for *ex vivo* biodistribution. All organs were collected, weighed, and their activity content measured in a gamma-counter. Tissue uptake of the radio-peptides was calculated as a percent of injected dose per gram tissue (%ID/g). The signal from the thyroid was removed from the analysis since it was not possible to distinguish between free  $^{125}\text{I}$  derived from the peptide degradation, naturally accumulated by the thyroid and  $^{125}\text{I}$ -labeled HE25 actually uptaken by the thyroid.

#### Biosafety study

SARS-CoV-2 siRNA/HE25 complexes were prepared at molar ratios of 1:20, 1:40, 1:80, and 1:100, according to the protocol described above and administered to Balb/c mice, using a dosage of 0.2 mg/kg. The administration was conducted either through i.v. injection or via nose-to-lung delivery. This regimen was repeated biweekly over a period of 15 days and mice were weighed every 5 days. At the end of the experiment, mice were subjected to carbon dioxide euthanasia, lungs were excised, and fixed in 10% formalin for 48 h, washed with PBS, and sectioned. Sections were processed using the Masson's Trichrome staining technique, adhering to the established protocol for this method, imaged by light microscopy, and analyzed by using FIJI ImageJ (NIH) plugin color deconvolution<sup>71,73</sup>.

#### Statistical analysis

Statistical analysis was assisted by GraphPad Prism software. Data from nanotracking analysis, zeta-potential, GAPDH silencing, and immunofluorescence colocalization experiments were analyzed by two-way ANOVA followed by multiple comparisons. Data from SARS-CoV-2 plaque assay were analyzed by two-way ANOVA followed by multiple comparisons for omicron BA.5 variant and one-way ANOVA for ancestral variant. Data from RT-qPCR experiments were analyzed by two-way ANOVA followed by multiple comparisons, and one-sample t test was additionally employed to evaluate the distance of RdRp remaining expression from 100%. Data from Masson Trichrome stainings of the biosafety study were analyzed by two-tailed unpaired t test.

#### DATA AND CODE AVAILABILITY

Data reported in this paper and any additional information required to reanalyze the data will be shared by the corresponding author upon

request. The figures of this manuscript are accessible to color-blind readers.

#### SUPPLEMENTAL INFORMATION

Supplemental information can be found online at <https://doi.org/10.1016/j.omtn.2024.102227>.

#### ACKNOWLEDGMENTS

We thank Line Lundegård Bang from Department of Clinical Microbiology, Odense University Hospital, for providing protocols and technical suggestions for the virus plaque assay on Vero E6 cells; Christina Baun from Department of Nuclear Medicine, Odense University Hospital, for performing the SPECT/CT scans and the biodistribution experiments; the Animal Core Facility at University of Southern Denmark for animal care; Anders Grønnegaard Schlosser from Department of Molecular Medicine, University of Southern Denmark, for providing protein FIB and anti-FIB antibody; Eva Kildall Hejbøl from the Department of Pathology, Odense University Hospital, for technical assistance with the transmission electron microscopy imaging; Jesper Bonnet Møller from the Department of Molecular Medicine, University of Southern Denmark, for assistance with the *in vivo* fluorescent complex transfection; Lone Christiansen Hejbøl from the Department of Pathology, Odense University Hospital, for technical assistance with the preparation of lung sections for microscopy; and Kat Occhipinti for editorial assistance. This study was partially supported by Novo Nordisk Foundation (NNF21OC0072274), NEYE-Fonden, A.P. Møller og Hustru Chastine Mc-Kinney Møllers Fond, Dagmar Marshalls Fond, Fabrikant Einar Willumsens Mindelegat, and Direktør Michael Hermann Nielsens Mindelegat, Afd. B. Funders did not contribute to the design, data acquisition, data analyses and interpretation, in the writing of the manuscript or in the decision to which journal to submit the manuscript for publication.

#### AUTHOR CONTRIBUTIONS

M.T. designed the HE25 peptide and performed most experiments, data interpretation, critical revision, and writing the manuscript draft. S.T.D.P. performed part of the siRNA/ $^{125}\text{I}$  HE25 transfections, all the plaque assays for SARS-CoV-2 infectivity and contributed to data interpretation. M.G.T. contributed to data interpretation and experimental design and performed part of the *in vivo* experiments. V.C.C. performed part of the EMSA, ELISA, and serum stability assays. N.K. and S.V. performed the Nano Tracking Analysis and zeta potential measurements. U.M.H. performed part of the confocal image acquisition using the Nikon microscope. N.L. performed the  $^{125}\text{I}$ -labeling of HE25 and contributed to data interpretation. H.T. contributed to the design of the *in vivo* SPECT/CT and biodistribution experiments. H.D.S. performed the transmission electron microscopy imaging. Y.P. contributed to the design of the plaque assays. H.J.D. mentored the study and contributed to data interpretation, experimental design, and made substantial contributions to manuscript writing and editing. The manuscript underwent review and editing by all of the authors.

## DECLARATION OF INTERESTS

The authors declare no competing interests.

## REFERENCES

- Carriero, V., De Paola, M., and Gioia, F. (2021). The health-economy trade-off during the Covid-19 pandemic: Communication matters. *PLoS One* 16, e0256103. <https://doi.org/10.1371/journal.pone.0256103>.
- V'Kovski, P., Kratzel, A., Steiner, S., Stalder, H., and Thiel, V. (2021). Coronavirus biology and replication: implications for SARS-CoV-2. *Nat. Rev. Microbiol.* 19, 155–170. <https://doi.org/10.1038/s41579-020-00468-6>.
- Wu, Z., Han, Z., Liu, B., and Shen, N. (2022). Remdesivir in treating hospitalized patients with COVID-19: A renewed review of clinical trials. *Front. Pharmacol.* 13, 971890. <https://doi.org/10.3389/fphar.2022.971890>.
- Matthews, D.B. (2020). A cocktail of antibodies for COVID-19 therapy. *Nat. Rev. Immunol.* 20, 591. <https://doi.org/10.1038/s41577-020-00431-9>.
- Hajjo, R., Sabbah, D.A., and Bardaweel, S.K. (2020). Chemocentric Informatics Analysis: Dexamethasone Versus Combination Therapy for COVID-19. *ACS Omega* 5, 29765–29779. <https://doi.org/10.1021/acscomega.0c03597>.
- Xie, X., Jiang, Y., Zeng, Y., and Liu, H. (2020). Combination antiviral therapy with lopinavir/ritonavir, arbidol and interferon- $\alpha$ 1b for COVID-19. *Antivir. Ther.* 25, 233–239. <https://doi.org/10.3851/IMP3362>.
- Wong, A. (2020). COVID-19 and toxicity from potential treatments: Panacea or poison. *Emerg. Med. Australasia (EMA)* 32, 697–699. <https://doi.org/10.1111/1742-6723.13537>.
- Akinbolade, S., Coughlan, D., Fairbairn, R., McConkey, G., Powell, H., Ogunbayo, D., and Craig, D. (2022). Combination therapies for COVID-19: An overview of the clinical trials landscape. *Br. J. Clin. Pharmacol.* 88, 1590–1597. <https://doi.org/10.1111/bcp.15089>.
- Ambike, S., Cheng, C.C., Feuerherd, M., Velkov, S., Baldassi, D., Afridi, S.Q., Porras-Gonzalez, D., Wei, X., Hagen, P., Kneidinger, N., et al. (2022). Targeting genomic SARS-CoV-2 RNA with siRNAs allows efficient inhibition of viral replication and spread. *Nucleic Acids Res.* 50, 333–349. <https://doi.org/10.1093/nar/gkab1248>.
- Idris, A., Davis, A., Supramaniam, A., Acharya, D., Kelly, G., Tayyar, Y., West, N., Zhang, P., McMillan, C.L.D., Soemardy, C., et al. (2021). A SARS-CoV-2 targeted siRNA-nanoparticle therapy for COVID-19. *Mol. Ther.* 29, 2219–2226. <https://doi.org/10.1016/j.ymthe.2021.05.004>.
- Malik, J.A., Ahmed, S., Mir, A., Shinde, M., Bender, O., Alshammari, F., Ansari, M., and Anwar, S. (2022). The SARS-CoV-2 mutations versus vaccine effectiveness: New opportunities to new challenges. *J. Infect. Public Health* 15, 228–240. <https://doi.org/10.1016/j.jiph.2021.12.014>.
- Bhattacharya, D., and Victora, G.D. (2022). Boosting with updated COVID-19 mRNA vaccines. *Nat. Med.* 28, 2257–2258. <https://doi.org/10.1038/s41591-022-02048-y>.
- Yazdani, M., Jafari, A., Mahdian, S., Namazi, M., and Gharaghani, S. (2023). Rational approaches to discover SARS-CoV-2/ACE2 interaction inhibitors: Pharmacophore-based virtual screening, molecular docking, molecular dynamics and binding free energy studies. *J. Mol. Liq.* 375, 121345. <https://doi.org/10.1016/j.molliq.2023.121345>.
- Tumskiy, R.S., Tumskaia, A.V., Klochkova, I.N., and Richardson, R.J. (2023). SARS-CoV-2 proteases Mpro and PLpro: Design of inhibitors with predicted high potency and low mammalian toxicity using artificial neural networks, ligand-protein docking, molecular dynamics simulations, and ADMET calculations. *Comput. Biol. Med.* 153, 106449. <https://doi.org/10.1016/j.combiomed.2022.106449>.
- Boytz, R., Slabicki, M., Ramaswamy, S., Patten, J.J., Zou, C., Meng, C., Hurst, B.L., Wang, J., Nowak, R.P., Yang, P.L., et al. (2023). Anti-SARS-CoV-2 activity of targeted kinase inhibitors: Repurposing clinically available drugs for COVID-19 therapy. *J. Med. Virol.* 95, e28157. <https://doi.org/10.1002/jmv.28157>.
- Khaitov, M., Nikonova, A., Shilovskiy, I., Kozhikhova, K., Kofiadi, I., Vishnyakova, L., Nikolskii, A., Gattinger, P., Kovchina, V., Barvinskaia, E., et al. (2021). Silencing of SARS-CoV-2 with modified siRNA-peptide dendrimer formulation. *Allergy* 76, 2840–2854. <https://doi.org/10.1111/all.14850>.
- Zhu, W., Chen, C.Z., Gorshkov, K., Xu, M., Lo, D.C., and Zheng, W. (2020). RNA-Dependent RNA Polymerase as a Target for COVID-19 Drug Discovery. *SLAS Discov.* 25, 1141–1151. <https://doi.org/10.1177/2472555220942123>.
- Friedrich, M., and Aigner, A. (2022). Therapeutic siRNA: State-of-the-Art and Future Perspectives. *BioDrugs* 36, 549–571. <https://doi.org/10.1007/s40259-022-00549-3>.
- Xia, H., Gu, G., Hu, Q., Liu, Z., Jiang, M., Kang, T., Miao, D., Song, Q., Yao, L., Tu, Y., et al. (2013). Activatable cell penetrating peptide-conjugated nanoparticles with enhanced permeability for site-specific targeting delivery of anticancer drug. *Bioconjugate Chem.* 24, 419–430. <https://doi.org/10.1021/bc300520t>.
- Steel, R., Cowan, J., Payerne, E., O'Connell, M.A., and Searcey, M. (2012). Anti-inflammatory Effect of a Cell-Penetrating Peptide Targeting the Nrf2/Keap1 Interaction. *ACS Med. Chem. Lett.* 3, 407–410. <https://doi.org/10.1021/ml300041g>.
- Higa, M., Katagiri, C., Shimizu-Okabe, C., Tsumuraya, T., Sunagawa, M., Nakamura, M., Ishiuchi, S., Takayama, C., Kondo, E., and Matsushita, M. (2015). Identification of a novel cell-penetrating peptide targeting human glioblastoma cell lines as a cancer-homing transporter. *Biochem. Biophys. Res. Commun.* 457, 206–212. <https://doi.org/10.1016/j.bbrc.2014.12.089>.
- Gao, H., Yang, Z., Zhang, S., Cao, S., Pang, Z., Yang, X., and Jiang, X. (2013). Glioma-homing peptide with a cell-penetrating effect for targeting delivery with enhanced glioma localization, penetration and suppression of glioma growth. *J. Contr. Release* 172, 921–928. <https://doi.org/10.1016/j.jconrel.2013.10.002>.
- Fei, L., Yap, L.P., Conti, P.S., Shen, W.C., and Zaro, J.L. (2014). Tumor targeting of a cell penetrating peptide by fusing with a pH-sensitive histidine-glutamate co-oligo-peptide. *Biomaterials* 35, 4082–4087. <https://doi.org/10.1016/j.biomaterials.2014.01.047>.
- Cerrato, C.P., Pirisinu, M., Vlachos, E.N., and Langel, Ü. (2015). Novel cell-penetrating peptide targeting mitochondria. *Faseb. J.* 29, 4589–4599. <https://doi.org/10.1096/fj.14-269225>.
- Tang, M., Zhang, X., Huang, Y., Cheng, W., Qu, J., Gui, S., Li, L., and Li, S. (2022). Peptide-based inhibitors hold great promise as the broad-spectrum agents against coronavirus. *Front. Microbiol.* 13, 1093646. <https://doi.org/10.3389/fmicb.2022.1093646>.
- Yan, R., Zhang, Y., Li, Y., Xia, L., Guo, Y., and Zhou, Q. (2020). Structural basis for the recognition of SARS-CoV-2 by full-length human ACE2. *Science* 367, 1444–1448. <https://doi.org/10.1126/science.abb2762>.
- Beyerstedt, S., Casaro, E.B., and Rangel, É.B. (2021). COVID-19: angiotensin-converting enzyme 2 (ACE2) expression and tissue susceptibility to SARS-CoV-2 infection. *Eur. J. Clin. Microbiol. Infect. Dis.* 40, 905–919. <https://doi.org/10.1007/s10096-020-04138-6>.
- Lan, J., Ge, J., Yu, J., Shan, S., Zhou, H., Fan, S., Zhang, Q., Shi, X., Wang, Q., Zhang, L., and Wang, X. (2020). Structure of the SARS-CoV-2 spike receptor-binding domain bound to the ACE2 receptor. *Nature* 581, 215–220. <https://doi.org/10.1038/s41586-020-2180-5>.
- Robles, J.P., Zamora, M., Adan-Castro, E., Siqueiros-Marquez, L., Martinez de la Escalera, G., and Clapp, C. (2022). The spike protein of SARS-CoV-2 induces endothelial inflammation through integrin  $\alpha$ 5 $\beta$ 1 and NF- $\kappa$ B signaling. *J. Biol. Chem.* 298, 101695. <https://doi.org/10.1016/j.jbc.2022.101695>.
- Nader, D., Fletcher, N., Curley, G.F., and Kerrigan, S.W. (2021). SARS-CoV-2 uses major endothelial integrin  $\alpha$ v $\beta$ 3 to cause vascular dysregulation in-vitro during COVID-19. *PLoS One* 16, e0253347. <https://doi.org/10.1371/journal.pone.0253347>.
- Tresoldi, I., Sanguolo, C.F., Manzari, V., and Modesti, A. (2020). SARS-COV-2 and infectivity: Possible increase in infectivity associated to integrin motif expression. *J. Med. Virol.* 92, 1741–1742. <https://doi.org/10.1002/jmv.25831>.
- Sigrist, C.J., Bridge, A., and Le Mercier, P. (2020). A potential role for integrins in host cell entry by SARS-CoV-2. *Antivir. Res.* 177, 104759. <https://doi.org/10.1016/j.antiviral.2020.104759>.
- Cantuti-Castelvetri, L., Ojha, R., Pedro, L.D., Djannatian, M., Franz, J., Kuivainen, S., van der Meer, F., Kallio, K., Kaya, T., Anastasina, M., et al. (2020). Neuropilin-1 facilitates SARS-CoV-2 cell entry and infectivity. *Science* 370, 856–860. <https://doi.org/10.1126/science.abd2985>.
- Bollavaram, K., Leeman, T.H., Lee, M.W., Kulkarni, A., Upshaw, S.G., Yang, J., Song, H., and Platt, M.O. (2021). Multiple sites on SARS-CoV-2 spike protein are

- susceptible to proteolysis by cathepsins B, K, L, S, and V. *Protein Sci.* 30, 1131–1143. <https://doi.org/10.1002/pro.4073>.
35. Padmanabhan, P., Desikan, R., and Dixit, N.M. (2020). Targeting TMPRSS2 and Cathepsin B/L together may be synergistic against SARS-CoV-2 infection. *PLoS Comput. Biol.* 16, e1008461. <https://doi.org/10.1371/journal.pcbi.1008461>.
  36. Tuttolomondo, M., Hansen, P.L., Mollenhauer, J., and Ditzel, H.J. (2018). One-step FPLC-size-exclusion chromatography procedure for purification of rDMBT1 6 kb with increased biological activity. *Anal. Biochem.* 542, 16–19. <https://doi.org/10.1016/j.ab.2017.11.015>.
  37. Casella, C., Tuttolomondo, M., Hoiland-Carlsen, P.F., and Mollenhauer, J. (2014). Natural pattern recognition mechanisms at epithelial barriers and potential use in nanomedicine. *Eur. J. Nanomed.* 6, 141–155. <https://doi.org/10.1515/ejnm-2014-0020>.
  38. Tuttolomondo, M., Casella, C., Hansen, P.L., Polo, E., Herda, L.M., Dawson, K.A., Ditzel, H.J., and Mollenhauer, J. (2017). Human DMBT1-Derived Cell-Penetrating Peptides for Intracellular siRNA Delivery. *Mol. Ther. Nucleic Acids* 8, 264–276. <https://doi.org/10.1016/j.omtn.2017.06.020>.
  39. Tuttolomondo, M., and Ditzel, H.J. (2021). Non-covalent Encapsulation of siRNA with Cell-Penetrating Peptides. *Methods Mol. Biol.* 2282, 353–376. [https://doi.org/10.1007/978-1-0716-1298-9\\_19](https://doi.org/10.1007/978-1-0716-1298-9_19).
  40. Tuttolomondo, M., and Ditzel, H.J. (2020). Simple FRET Electrophoresis Method for Precise and Dynamic Evaluation of Serum siRNA Stability. *ACS Med. Chem. Lett.* 11, 195–202. <https://doi.org/10.1021/acsmchemlett.9b00472>.
  41. Tuttolomondo, M., and Ditzel, H.J. (2021). Evaluation of siRNA Stability and Interaction with Serum Components Using an Agarose Gel-Based Single-Molecule FRET Labeling Method. *Methods Mol. Biol.* 2282, 43–56. [https://doi.org/10.1007/978-1-0716-1298-9\\_4](https://doi.org/10.1007/978-1-0716-1298-9_4).
  42. Wang, R., Shen, Q., Li, X., Xie, C., Lu, W., Wang, S., Wang, J., Wang, D., and Liu, M. (2018). Efficacy of inverse isomer of CendR peptide on tumor tissue penetration. *Acta Pharm. Sin. B* 8, 825–832. <https://doi.org/10.1016/j.apsb.2018.06.006>.
  43. Hashimoto, R., Sakamoto, A., Deguchi, S., Yi, R., Sano, E., Hotta, A., Takahashi, K., Yamana, S., and Takayama, K. (2021). Dual inhibition of TMPRSS2 and Cathepsin B prevents SARS-CoV-2 infection in iPS cells. *Mol. Ther. Nucleic Acids* 26, 1107–1114. <https://doi.org/10.1016/j.omtn.2021.10.016>.
  44. Akinc, A., Querbes, W., De, S., Qin, J., Frank-Kamenetsky, M., Jayaprakash, K.N., Jayaraman, M., Rajeev, K.G., Cantley, W.L., Dorkin, J.R., et al. (2010). Targeted Delivery of RNAi Therapeutics With Endogenous and Exogenous Ligand-Based Mechanisms. *Mol. Ther.* 18, 1357–1364. <https://doi.org/10.1038/mt.2010.85>.
  45. Kanasty, R.L., Whitehead, K.A., Vegas, A.J., and Anderson, D.G. (2012). Action and Reaction: The Biological Response to siRNA and Its Delivery Vehicles. *Mol. Ther.* 20, 513–524. <https://doi.org/10.1038/mt.2011.294>.
  46. Gan, B.K., Yong, C.Y., Ho, K.L., Omar, A.R., Alitheen, N.B., and Tan, W.S. (2018). Targeted Delivery of Cell Penetrating Peptide Virus-like Nanoparticles to Skin Cancer Cells. *Sci. Rep.* 8, 8499. <https://doi.org/10.1038/s41598-018-26749-y>.
  47. Xie, J., Bi, Y., Zhang, H., Dong, S., Teng, L., Lee, R.J., and Yang, Z. (2020). Cell-Penetrating Peptides in Diagnosis and Treatment of Human Diseases: From Preclinical Research to Clinical Application. *Front. Pharmacol.* 11, 697. <https://doi.org/10.3389/fphar.2020.00697>.
  48. Zhang, L., Xu, J., Wang, F., Ding, Y., Wang, T., Jin, G., Martz, M., Gui, Z., Ouyang, P., and Chen, P. (2019). Histidine-Rich Cell-Penetrating Peptide for Cancer Drug Delivery and Its Uptake Mechanism. *Langmuir* 35, 3513–3523. <https://doi.org/10.1021/acs.langmuir.8b03175>.
  49. Upadhyay, A., and Sangave, P.C. (2016). Hydrophobic and electrostatic interactions between cell penetrating peptides and plasmid DNA are important for stable non-covalent complexation and intracellular delivery. *J. Pept. Sci.* 22, 647–659. <https://doi.org/10.1002/psc.2927>.
  50. Walrant, A., Bauzá, A., Girardet, C., Alves, I.D., Lecomte, S., Illien, F., Cardon, S., Chaianantakul, N., Pallerla, M., Burlina, F., et al. (2020). Ionpair- $\pi$  interactions favor cell penetration of arginine/tryptophan-rich cell-penetrating peptides. *Biochim. Biophys. Acta Biomembr.* 1862, 183098. <https://doi.org/10.1016/j.bbmem.2019.183098>.
  51. Wu, M., Guo, H., Liu, L., Liu, Y., and Xie, L. (2019). Size-dependent cellular uptake and localization profiles of silver nanoparticles. *Int. J. Nanomed.* 14, 4247–4259. <https://doi.org/10.2147/IJN.S201107>.
  52. Zhang, D., Wei, L., Zhong, M., Xiao, L., Li, H.W., and Wang, J. (2018). The morphology and surface charge-dependent cellular uptake efficiency of upconversion nanostructures revealed by single-particle optical microscopy. *Chem. Sci.* 9, 5260–5269. <https://doi.org/10.1039/c8sc01828f>.
  53. Zhang, W., Taheri-Ledari, R., Ganjali, F., Mirmohammadi, S.S., Qazi, F.S., Saaidirad, M., KashtiAray, A., Zarei-Shokat, S., Tian, Y., and Maleki, A. (2022). Effects of morphology and size of nanoscale drug carriers on cellular uptake and internalization process: a review. *RSC Adv.* 13, 80–114. <https://doi.org/10.1039/d2ra06888e>.
  54. Hong, Y., Hu, F.Q., and Yuan, H. (2006). Effect of PEG2000 on drug delivery characterization from solid lipid nanoparticles. *Pharmazie* 61, 312–315.
  55. Ludwig, B.S., Kessler, H., Kossatz, S., and Reuning, U. (2021). RGD-Binding Integrins Revisited: How Recently Discovered Functions and Novel Synthetic Ligands (Re-)Shape an Ever-Evolving Field. *Cancers* 13, 1711. <https://doi.org/10.3390/cancers13071711>.
  56. Teo, S.L.Y., RENNICK, J.J., Yuen, D., Al-Wassiti, H., Johnston, A.P.R., and Pouton, C.W. (2021). Unravelling cytosolic delivery of cell penetrating peptides with a quantitative endosomal escape assay. *Nat. Commun.* 12, 3721. <https://doi.org/10.1038/s41467-021-23997-x>.
  57. Smith, S.A., Selby, L.I., Johnston, A.P.R., and Such, G.K. (2019). The Endosomal Escape of Nanoparticles: Toward More Efficient Cellular Delivery. *Bioconjugate Chem.* 30, 263–272. <https://doi.org/10.1021/acs.bioconjchem.8b00732>.
  58. Zhong, Y.J., Shao, L.H., and Li, Y. (2013). Cathepsin B-cleavable doxorubicin prodrugs for targeted cancer therapy (Review). *Int. J. Oncol.* 42, 373–383. <https://doi.org/10.3892/ijo.2012.1754>.
  59. Wojnilowicz, M., Glab, A., Bertucci, A., Caruso, F., and Cavalieri, F. (2019). Super-resolution Imaging of Proton Sponge-Triggered Rupture of Endosomes and Cytosolic Release of Small Interfering RNA. *ACS Nano* 13, 187–202. <https://doi.org/10.1021/acsnano.8b05151>.
  60. Egorova, E.A., and Nikitin, M.P. (2022). Delivery of Theranostic Nanoparticles to Various Cancers by Means of Integrin-Binding Peptides. *Int. J. Mol. Sci.* 23, 13735. <https://doi.org/10.3390/ijms232213735>.
  61. Teesalu, T., Sugahara, K.N., Kotamraju, V.R., and Ruoslahti, E. (2009). C-end rule peptides mediate neuropilin-1-dependent cell, vascular, and tissue penetration. *Proc. Natl. Acad. Sci. USA* 106, 16157–16162. <https://doi.org/10.1073/pnas.0908201106>.
  62. Teoh, C.M., Tan, S.S.L., and Tran, T. (2015). Integrins as Therapeutic Targets for Respiratory Diseases. *Curr. Mol. Med.* 15, 714–734. <https://doi.org/10.2174/1566524015666150921105339>.
  63. Wang, C., Gu, S., Yin, X., Xiang, Z., Li, Z., Cao, H., Meng, X., Hu, K., and Han, X. (2016). The toxic effects of microcystin-LR on mouse lungs and alveolar type II epithelial cells. *Toxicol. 115*, 81–88. <https://doi.org/10.1016/j.toxicol.2016.03.007>.
  64. Iacob, S., and Iacob, D.G. (2020). SARS-CoV-2 Treatment Approaches: Numerous Options, No Certainty for a Versatile Virus. *Front. Pharmacol.* 11, 1224. <https://doi.org/10.3389/fphar.2020.01224>.
  65. Zhang, W., Pei, J., and Lai, L. (2017). Computational Multitarget Drug Design. *J. Chem. Inf. Model.* 57, 403–412. <https://doi.org/10.1021/acs.jcim.6b00491>.
  66. Jumper, J., Evans, R., Pritzel, A., Green, T., Figurnov, M., Ronneberger, O., Tunyasuvunakool, K., Bates, R., Židek, A., Potapenko, A., et al. (2021). Highly accurate protein structure prediction with AlphaFold. *Nature* 596, 583–589. <https://doi.org/10.1038/s41586-021-03819-2>.
  67. Li, H., Huang, E., Zhang, Y., Huang, S.Y., and Xiao, Y. (2022). HDock update for modeling protein-RNA/DNA complex structures. *Protein Sci.* 31, e4441. <https://doi.org/10.1002/pro.4441>.
  68. Pettersen, E.F., Goddard, T.D., Huang, C.C., Couch, G.S., Greenblatt, D.M., Meng, E.C., and Ferrin, T.E. (2004). UCSF Chimera—a visualization system for exploratory research and analysis. *J. Comput. Chem.* 25, 1605–1612. <https://doi.org/10.1002/jcc.20084>.
  69. Delenclos, M., Trendafilova, T., Mahesh, D., Baine, A.M., Moussaud, S., Yan, I.K., Patel, T., and McLean, P.J. (2017). Investigation of Endocytic Pathways for the

- Internalization of Exosome-Associated Oligomeric Alpha-Synuclein. *Front. Neurosci.* 11, 172. <https://doi.org/10.3389/fnins.2017.00172>.
70. Pedersen, R.M., Bang, L.L., Tornby, D.S., Kierkegaard, H., Nilsson, A.C., Johansen, I.S., Bistrup, C., Jensen, T.G., Justesen, U.S., and Andersen, T.E. (2021). The SARS-CoV-2-neutralizing capacity of kidney transplant recipients 4 weeks after receiving a second dose of the BNT162b2 vaccine. *Kidney Int.* 100, 1129–1131. <https://doi.org/10.1016/j.kint.2021.09.006>.
71. Schindelin, J., Arganda-Carreras, I., Frise, E., Kaynig, V., Longair, M., Pietzsch, T., Preibisch, S., Rueden, C., Saalfeld, S., Schmid, B., et al. (2012). Fiji: an open-source platform for biological-image analysis. *Nat. Methods* 9, 676–682. <https://doi.org/10.1038/nmeth.2019>.
72. Bolte, S., and Cordelières, F.P. (2006). A guided tour into subcellular colocalization analysis in light microscopy. *J. Microsc.* 224, 213–232. <https://doi.org/10.1111/j.1365-2818.2006.01706.x>.
73. Landini, G., Martinelli, G., and Piccinini, F. (2021). Colour deconvolution: stain unmixing in histological imaging. *Bioinformatics* 37, 1485–1487. <https://doi.org/10.1093/bioinformatics/btaa847>.